

# Characterizing BDS signal-in-space performance from integrity perspective

Shizhuang Wang  | Yawei Zhai  | Xingqun Zhan 

School of Aeronautics and Astronautics,  
Shanghai Jiao Tong University, Shanghai,  
China

## Correspondence

Xingqun Zhan, School of Aeronautics  
and Astronautics, Shanghai Jiao Tong  
University, Shanghai, China.

## Funding information

China Postdoctoral Science Foundation,  
Grant/Award Numbers: 2019, M661511

## Abstract

The full deployment of China's BeiDou navigation satellite system (BDS) was finalized in June 2020. To support safety-critical applications, the system must provide assured signal-in-space (SIS) performance. As one of the key steps forward for BDS, this paper characterizes the SIS range errors (SISREs) for both the regional (BDS-2) and the global (BDS-3) systems from the integrity perspective. Following the safety standards in aviation, a data-driven SISRE evaluation scheme is presented in this work. This scheme evaluates the overbounding user range accuracy (URA) and the prior fault probability to respectively capture the nominal and anomalous SIS behaviors. By processing the 4.5-year ephemerides starting from 2016 for BDS-2 and the recent 1.5-year data from 2019 for BDS-3, we preliminarily provide an overall picture of the BDS SIS characteristics and reveal the significant performance variation among different satellites.

## 1 | INTRODUCTION

As one of the “Big 4” core constellations, China's BeiDou navigation satellite system (BDS) has been incrementally evolved in recent years (Yang, Gao, Guo, Mao, & Yang, 2019). Since December 2012, the regional BDS (BDS-2) has been offering positioning, navigation, and timing (PNT) services to the Asia-Pacific users with 14 satellites that are sparsely distributed in geostationary orbit (GEO), inclined geostationary orbit (IGSO), and medium Earth orbit (MEO) (China Satellite Navigation Office [CSNO], 2019a). Then, the deployment of the global system (BDS-3) was started in 2015 and finalized in June 2020. The new constellation (BDS-3) can offer global PNT services with 30 new satellites in space, including 3 GEOs, 3 IGSOs, and 24 MEOs (CSNO, 2019a). As a member of Global Navigation Satellite Systems (GNSS), BDS is expected to bring significant benefits to users by enhancing navigation accuracy, integrity, continuity, and availability.

The quality of PNT services highly depends on the constellation's signal-in-space (SIS) performance. The SIS performance is typically characterized by evaluating the

associated SIS range error (SISRE). SISRE describes the equivalent pseudorange error mainly originating from the ephemeris and clock errors of a satellite and is one of the main error sources that influence the positioning accuracy and integrity (Wu et al., 2017).

SISRE is also an important constellation performance indicator that is jointly driven by both the space segment characteristics and the control segment capabilities (Montenbruck, Steigenberger, et al., 2015). Therefore, the following features of BDS can significantly impact its SISRE behaviors. First, its space segment is composed of MEO, IGSO, and GEO satellites, for which the orbital motion predictability is different. Second, the satellite clock stability differs significantly between BDS-2 and BDS-3. Besides, the broadcast orbit and clock parameters are separately determined by orbit determination and time synchronization (OD & TS) and two-way satellite time and frequency transfer (TWSTFT) (Lv, Geng, Zhao, & Liu, 2018; Wu et al., 2017), which weakens the correlation between orbit errors and clock errors. Furthermore, BDS-3 employs the inter-satellite links (ISLs) to mitigate the challenges caused by limited ground stations, and thus,

the associated SIS accuracy can be improved (Yang et al., 2019).

As BDS becomes mature, there is an increasing desire to combine it with other constellations for supporting safety-critical applications, such as aviation. The prerequisite to achieve this goal is a proper quantification of navigation integrity. Integrity measures the trust that can be placed on the correctness of the navigation information (Zhu, Marais, Betaille, & Berbineau, 2018) and has been regarded as a key performance criterion in aviation for a long time. The aviation community is now pursuing Advanced Receiver Autonomous Integrity Monitoring (RAIM) to support aircraft precision approaching procedures (Blanch et al., 2015). To assure navigation integrity, RAIM requires a ground monitor to provide the aircraft with some integrity-related parameters through the Integrity Support Message (ISM) (Martini & Sgammini, 2019; Perea, Meurer, Martini, et al., 2018; Walter, Blanch, & Gunning, 2019).

User range accuracy (URA) and prior fault probability are two essential integrity parameters within the ISM, which respectively capture the nominal and anomalous SISRE behaviors. As a key step toward promoting BDS in civil aviation, China has been devoting continuous efforts to drafting the BDS standards under the International Civil Aviation Organization (ICAO), including committing these two parameters. And it is expected that BDS will be included in the ICAO Standard and Recommended Practices (SARPs) by the end of 2020 (CSNO, 2019b).

This paper aims at providing preliminary estimates of the ISM parameters for both BDS-2 and BDS-3. There have been some prior efforts investigating SISRE characterization for GPS, GLONASS, and Galileo. Heng, Gao, Walter, & Enge (2011) studied the GPS SIS performance between 2008 and 2010 with an emphasis on the nominal error behaviors. Later, the GPS SIS anomalies between 2000 and 2010 were investigated by comparing the broadcast and precise ephemerides (Heng, Gao, Walter, & Enge, 2012). After RAIM was proposed, some further studies were conducted to estimate or validate the ISM parameters for GPS (Perea, Meurer, Rippl, Belabbas, & Joerger, 2017; Walter & Blanch, 2015; Walter, Gunning, Eric Phelts, & Blanch, 2018), and similar analyses were carried out for GLONASS (Heng et al., 2012; Walter et al., 2018) and Galileo (Martini, Sgammini, & Boyero, 2020a; Perea et al., 2017). Montenbruck, Steigenberger, et al. (2015) performed a consistent analysis of nominal SISREs for all available constellations over a 12-month period in 2013/2014. This study was extended to analyze the data in 2017, where additional constellation-specific SISRE evaluation criteria were addressed (Montenbruck, Steigenberger, & Hauschild, 2018). As for BDS-2, some studies have investigated its nominal SIS behaviors (Wang, Shao, Li, Song,

& Li, 2018; Wu et al., 2017) and its SIS anomalies (Ouyang et al., 2019). To the best of our knowledge, few studies have focused on characterizing the SISREs of BDS-3 from the integrity perspective, although there were some preliminary assessments on its SIS accuracy (Lv, Geng, Zhao, Xie, & Zhou, 2020; Montenbruck, Steigenberger, & Hauschild, 2020).

As for the prior studies on evaluating the BDS-2 SISREs, their associated results cannot be used to support future RAIM adoption. This is because, first, they evaluated the URAs by merely overbounding the core (i.e., 68%) error distribution, which could lead to an overly optimistic estimate. Second, little attention has been paid to the mean-time-to-notify (MTTN), which describes the average fault duration, but this indicator is essential for fault probability determination. Third, the definition of SIS faults was either absent or inconsistent with the safety standards in aviation (Walter, Blanch, and Gunning, 2019; Walter, Blanch, Joerger, & Pervan, 2019). In response, this work presents a new SISRE evaluation scheme by following these safety standards and characterizes the BDS SIS performance using this scheme.

The rest of this paper is organized as follows. Section 2 introduces the data sources and the SISRE computation procedures. Section 3 presents the definitions of SIS anomalies and the fault probability determination rationale. Then, Section 4 describes the methodology to analyze the nominal SIS performance. The BDS SIS behaviors are investigated in Section 5. Finally, Section 6 draws the conclusions.

## 2 | DATASETS AND SISRE EVALUATION METHODOLOGY

### 2.1 | Datasets and data cleaning

This study is carried out by employing the historical broadcast and precise ephemerides of BDS. The performance evaluation for BDS-2 is conducted over a 4.5-year period from 2016 to mid-2020 (June 21). And the analysis for BDS-3 only involves the recent 1.5-year data starting in 2019 due to the limited availability of BDS-3 precise products.

International GNSS Service (IGS) Multi-GNSS Experiment (MGEX) provides daily combined broadcast ephemerides (BCEs) by merging observed data from global GNSS tracking stations. This product, called BRDM, shows satisfactory continuity over the analysis period and thus is adopted as the primary BCE data source in this study. Besides, we utilize another two BCE products for data augmentation: the product from the Test and Assessment Research Center (TARC) of CSNO (available at: <http://www.csno-tarc.cn/en/support/downloads>) and the

product offered by Innovation Academy for Precision Measurement Science and Technology (APM), Chinese Academy of Sciences (CAS) (available at: <ftp://159.226.162.31>).

A sanity check is an important preprocessing step to remove data logging errors from the original records, which was implemented through a majority voting approach (Heng et al., 2012). However, this approach may be biased because the error patterns are highly sensitive to the hardware and software used in the stations (Montenbruck et al., 2018). In this work, the BRDM product is mostly employed for the analysis, which can overcome this shortcoming by adopting the following data cleaning strategy (O. Montenbruck, personal communication, July 10, 2019): first, it performs the least significant bit recovery for converting back to broadcast bits (Heng et al., 2012) and then removes the incorrect numbers due to rounding and truncation; second, the incomplete records are isolated; finally, different records at the same epoch are all retained in the final file if their correctness cannot be unambiguously judged.

To perform a reliable SISRE evaluation, we also need to identify which ephemeris is actually available to the navigation users at a specific epoch. For this purpose, the BCE products provide the transmission time of message ( $t_{tm}$ ) to indicate the time when an ephemeris was first received by the tracking stations. With this parameter, the ephemeris selection process was implemented as follows (Montenbruck et al., 2018): for a given epoch  $t$ , one should select the record that minimizes  $(t_{tm} - t)$  with the condition that  $(t_{tm} - t) \geq 0$ . However, this strategy is not well suited for integrity evaluation because it does not take incorrect records into account. In this work, we propose a new strategy by applying the following criteria (CSNO, 2019a):

- a. Normally, the orbit parameters are updated at the start of every BDT hour, and the reference time of ephemeris ( $t_{oe}$ ) is an integral point. The value of  $t_{oe}$  shall change if any of the orbit parameters change. Under abnormal conditions, the parameters may be updated at nonintegral points, and the value of  $t_{oe}$  will accordingly change. These rules also apply to the clock correction parameters.
- b. The health flag of a satellite can be updated at any time, and this will not influence the values of  $t_{oe}$  and  $t_{oc}$  (the reference time of clock parameters).

Based on the criteria above, one can judge whether there are incorrect records at a given epoch. If it proves that wrong records do exist, we then use a posterior approach to identify the correct message: multiple sets of orbit and clock parameters are separately derived using different

records, and the record that is most consistent with the precise product is regarded as the correct one. This method is initially acceptable because it is very unlikely that a faulted ephemeris (i.e., the satellite broadcast inaccurate information) coincidentally becomes consistent with the precise one after being disturbed by random recording errors. However, please note, this approach may lead to a selection bias that might hide true faults. A reliable approach should not depend on precise ephemerides, which will be further investigated in the future.

When selecting the ephemeris, we also take the applicability interval into consideration by applying the following rule: the ephemeris for use should be the one that minimizes  $(t_{oe} - t)$  subject to  $0 \leq (t_{oe} - t) \leq 1$  hour. An epoch should be labeled as “no BCE” if there is no correct record satisfying this condition. To reveal the possible causes of the missing BCEs and to prove the rationality of the rule above, we provide some further analyses as follows.

Normally, the broadcast ephemeris is updated at the start of every BDT hour, while it is missing for a few hours in the dataset. The absences may be caused by (a) the satellite encountered a signal outage (i.e., stopped signal transmission), (b) the tracking stations failed to record that message or the BCE products failed to restore it, or (c) the navigation message was not normally updated. To preliminarily identify the cause of each missing message, we employ the raw observation files from the MGEX stations for judging the pseudorange availability when the ephemeris was absent. The result suggests that most of the missing BCEs are likely caused by satellite signal outages because the pseudoranges were also unavailable over those periods. However, this is not true for a few absences occurring before mid-2017. At the current stage, we cannot unambiguously find the reason behind these absences, and we will conduct a more comprehensive analysis to account for every absence in the future.

In this study, the application interval of BDS ephemerides is set to one hour. This is justified because, as mentioned above, the missing BCEs are mostly caused by signal outages. Besides, it is abnormal that the ephemeris is not updated at the start of a BDT hour (CSNO, 2019a). Therefore, it is suggested that the expired ephemeris should not be used in safety-critical applications. This will potentially reduce the integrity risk at the cost of a slight increase in continuity risk.

The BDS precise ephemerides (PCEs) are routinely generated by several MGEX Analysis Centers (ACs) (Montenbruck et al., 2017). For the period of interest, two ACs continuously provide the final PCEs of all the BDS-2 satellites: WHU (Wuhan University) and GFZ (Geoforschungszentrum) (IGS MGEX, 2020a). In this study, WHU products are mostly employed for the BDS-2 SIS performance evaluation, and GFZ products are regarded as a

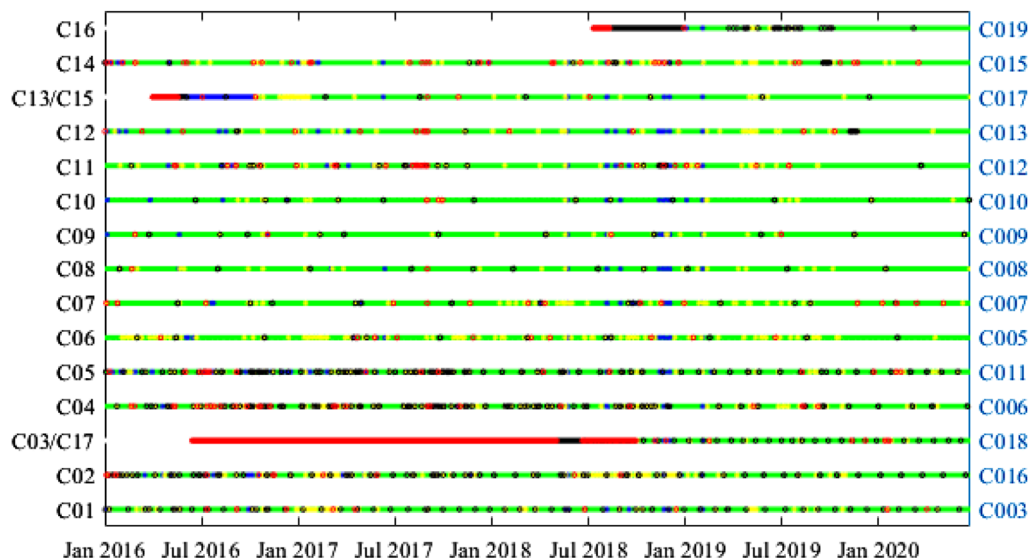


**FIGURE 1** Summary of observations for BDS-2 satellites, where green indicates good observations, blue and yellow indicate missing WHU and GFZ precise ephemerides respectively, black means the absence of PCEs, and red indicates no BCE. Note: the satellite C018 switched its PRN from C17 to C03 on 2018/09/29, and C017 switched its PRN from C15 to C13 on 2016/10/11 [Color figure can be viewed in the online issue, which is available at [wileyonlinelibrary.com](http://wileyonlinelibrary.com) and [www.ion.org](http://www.ion.org)]

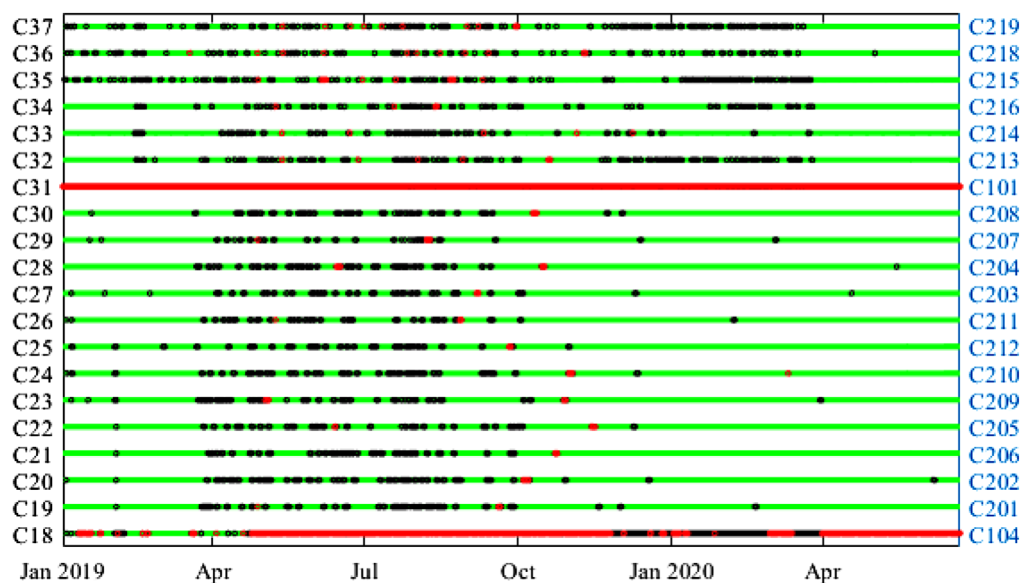


**FIGURE 2** Summary of observations for BDS-3 satellites, where green indicates good observations, black means missing PCE, and red indicates the absence of BCEs. Note: the satellites C18 and C31 are outside the nominal BDS-3 constellation [Color figure can be viewed in the online issue, which is available at [wileyonlinelibrary.com](http://wileyonlinelibrary.com) and [www.ion.org](http://www.ion.org)]

backup when the former has short breaks. As for BDS-3, only WHU can continuously provide the final PCEs over the analysis period. In this work, the sample interval of the precise products is 15 minutes. For an epoch, the PCE product for a satellite is deemed as invalid if the associated precise orbit or clock information is absent or invalid. The epochs when the two products are simultaneously invalid are labeled as “no PCE.” Appendix A gives some further

analyses on the missing PCEs, including their causes and the potential effects on the evaluation.

Figures 1 and 2 show the data status for individual satellites of BDS-2 and BDS-3. Due to the significant volume of missing data, the integrity performance of the satellites C03/C17, C16, C18, and C31-C37 is not evaluated in this study. The absence of precise products may be caused by the fact that the MGEX observations are likely to be limited



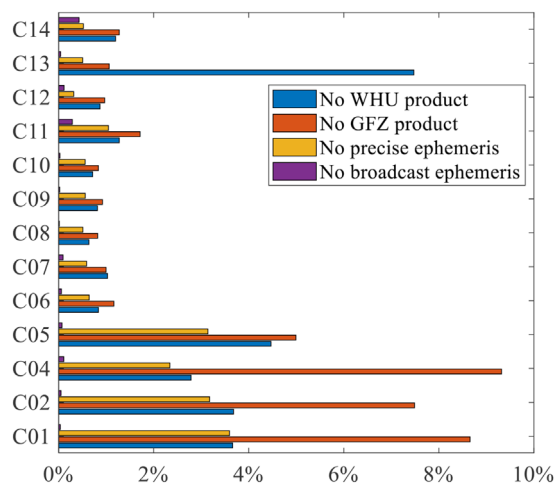


**FIGURE 3** The percentages of missing BCE and PCE products for BDS-2 satellites [Color figure can be viewed in the online issue, which is available at [wileyonlinelibrary.com](http://wileyonlinelibrary.com) and [www.ion.org](http://www.ion.org)]

for new satellites. And the continuous absence of BCEs for some satellites (e.g., C03/C17) may be due to one of the following reasons: (a) the MGEX stations may not track the newly launched satellites and those experimental satellites (e.g., C17, C18, C31) that are outside the nominal constellation, or (b) these satellites may not broadcast open-service navigation messages. The latter case exerts little effect on the integrity analysis because the navigation solution will not be affected by a satellite that does not broadcast navigation messages. Besides, it makes sense that the satellites outside the nominal constellation shall not be used in safety-critical applications. In this work, we also discard the observations of C13/C15 before 2017, considering that the stability of the satellite itself and of the precise products may be poor in the first several months after launch.

For the rest of the satellites, Figure 3 and Figure 4 present a direct view on their data unavailability percentage. The results suggest that despite the efforts devoted to data augmentation, a relatively large percentage of BCE and PCE products are absent. This will negatively impact the evaluation of the BDS integrity performance. Therefore, it is worth noting that the following analyses can only coarsely capture the characteristics of BDS SISREs, and we will conduct more rigorous evaluations by accounting for every absence in future work.

The precise products must be much more accurate than the BCEs to serve as the reference for SISRE evaluation. For BDS-2, prior studies have shown the feasibility of utilizing precise ephemerides in SISRE evaluation (Montenbruck et al., 2018; Yang, Xu, Nie, Gao, & Guan, 2019). As for BDS-3, the precise products of some satellites (including C19~C22 and C29~C30) achieve a 7-cm level radial orbit accuracy, while the products of other satellites may have poor quality due to limited tracking data (J. Guo, personal

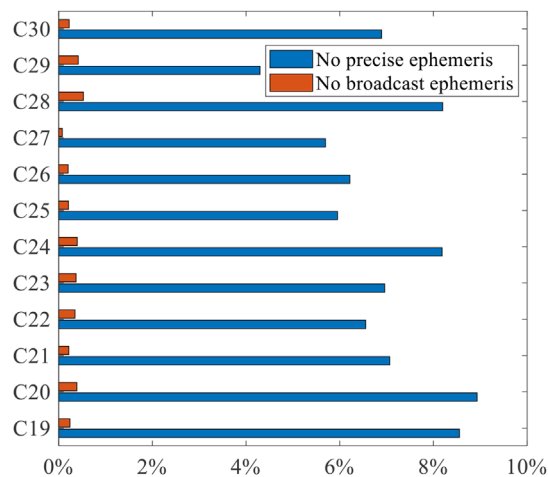


**FIGURE 4** The percentages of missing BCE and PCE products for BDS-3 satellites [Color figure can be viewed in the online issue, which is available at [wileyonlinelibrary.com](http://wileyonlinelibrary.com) and [www.ion.org](http://www.ion.org)]

communication, August 1, 2019). Therefore, only these six satellites will be involved in the preliminary BDS-3 SISRE evaluation.

## 2.2 | Time, coordinate, and corrections

Because the BCEs and PCEs are referred to the different time and coordinate systems, adequate care must be taken to ensure the consistency in the comparison. Aside from time and coordinate system alignment, several additional corrections are required in the data preprocessing procedures.

The BDS BCEs are referred to the Beidou time (BDT) scale, while the PCEs are given in the GPS time (GPST). In this study, GPST is selected as the basic time scale, and a 14-s BDT-GPST time offset is applied to the broadcast ephemerides. The synchronization error between GPST and BDT is in the order of 50 ns (CSNO, 2019a; Wang & Du, 2018), which can be ignored in the comparison between the broadcast orbits and the precise ones.

The broadcast and precise orbits are respectively specified in CGCS2000 and ITRF2008. However, the two frames are commonly considered to agree at few centimeters level (Montenbruck, Steigenberger, et al., 2015). Since this difference is well below the uncertainty of the BCE, it can be ignored in the following analysis. It is worth mentioning that BDS and GPS adopt a different geocentric gravitational constant and Earth's rotation rate, and incorrect substitution could lead to orbital errors up to several meters (Yang et al., 2019).

The satellite phase center offset (PCO) also significantly impacts the SISRE evaluation, which describes the location of the satellite's antenna phase center (APC)

relative to its center of mass (CoM). The PCEs generally provide the CoM orbit positions and the APC clock offsets, while the orbit and clock parameters derived from the BCEs are both referred to the APC. As an exception to this rule, the reference point of the broadcast orbits for BDS-2 was CoM before Day-Of-Year (DOY) 17, 2017 and was changed to the APC of B3I signal thereafter (B. Wang, Chen, Wang, & Zhou, 2018). Therefore, PCO corrections should be applied in the comparison between the broadcast and precise orbits after that day.

The PCO values of BDS-2 and BDS-3 satellites are generally provided in the satellite-fixed coordinate frame: the origin is the CoM of the satellite, the z-axis points toward the geocenter, the y-axis corresponds to the cross product of the z-axis with the satellite-Sun vector, and the x-axis completes the right-handed system (Montenbruck, Schmid, et al., 2015). Different PCOs are adopted by different MGEX ACs. For both BDS-2 and BDS-3, WHU used the manufacturer-provided PCOs (CSNO, 2019c) before GPS week 2072 and has been adopting the IGS official values included in *igs14.atx* (IGS MGEX, 2020b) since then. In the meantime, GFZ has been using the European Space Agency (ESA)-estimated BDS-2 PCO values (Dilssner, Springer, Schönemann, & Enderle, 2014). The broadcast orbit errors in Earth-centered Earth-fixed (ECEF) frame,  $[\Delta x \ \Delta y \ \Delta z]^T$ , are

$$\begin{bmatrix} \Delta x \\ \Delta y \\ \Delta z \end{bmatrix} = \begin{bmatrix} x \\ y \\ z \end{bmatrix}_b - \left( \begin{bmatrix} x \\ y \\ z \end{bmatrix}_p - A_S^E \cdot \begin{bmatrix} dx \\ dy \\ dz \end{bmatrix}_{\text{PCO}} \right), \quad (1)$$

where  $A_S^E$  denotes the attitude matrix describing the transformation from the satellite-fixed frame to ECEF;  $dx$ ,  $dy$ , and  $dz$  are the PCOs; and subscripts “b” and “p” respectively represent the BCEs and PCEs. In this work,  $A_S^E$  is calculated by assuming that the satellites adopt a nominal yaw-steering attitude mode, although the satellites sometimes switch to the orbit-normal attitude mode (Montenbruck, Schmid, et al., 2015). This is acceptable because adopting incorrect attitude modes can only cause a projected range error of about 15 cm at most for any point on the Earth (Montenbruck et al., 2018).

The BDS broadcast clock offset  $T_b^i$  of satellite  $i$  is referred to the APC of the B3I signal (CSNO, 2019a), while the precise clock offset  $T_p^i$  is referred to the equivalent APC of the dual-frequency ionosphere-free (IF) combination. Therefore, time group delay (TGD) correction  $T_{\text{GD}}^i$  should be applied to the broadcast clock offset for comparison with the precise product. In the BCEs, the TGD corrections for B1I/B3I and B2I/B3I are given in  $T_{\text{GD1}}^i$  and  $T_{\text{GD2}}^i$ , respectively. Please note, the errors of the broadcast TGDs contribute to the broadcast clock errors, and their effects

on the user ranging errors are accounted in the above process. Therefore, we do not additionally calculate the TGD errors using differential code biases (DCBs), and this is justified for the evaluation of the aforementioned dual-frequency users. However, in future work, we will evaluate the BDS TGD accuracy as Martini, Sgammini, and Boyero (2020b) do to support the users using single frequency or other dual-frequency combinations. Table 1 shows the associated TGD corrections for different precise products. Note that, since the relativistic effect is not corrected in the PCEs, the correction should also NOT be applied to the broadcast clock offsets. Accordingly, the difference between the broadcast and precise clock offsets is given by the following:

$$\delta T_b^i = T_b^i - T_{\text{GD}}^i - T_p^i. \quad (2)$$

Besides, there is a time-varying and satellite-independent timescale bias  $\mu$  (relative to GPST) in the reference clock of the PCEs. Therefore, at epoch  $k$ ,  $\delta T_b^i$  can be modeled as

$$\delta T_b^i(k) = \Delta T^i(k) + \mu(k), \quad (3)$$

where  $\Delta T^i(k)$  denotes the broadcast clock error for satellite  $i$ . To obtain  $\Delta T^i(k)$ , the bias term  $\mu(k)$  needs to be estimated. We adopt the robust iterative-weighted-average method (Wu et al., 2017) to realize the estimation because of its good tolerance to the potential clock outliers.

### 2.3 | Ephemeris status: Age-of-data, URA index, and health flag

The SIS accuracy is usually affected by the elapsed time since the generation of the orbit and clock information. The broadcast ephemeris employs age-of-data-ephemeris (AODE) and age-of-data-clock (AODC) to indicate how recent this navigation message is. Tables 2 and 3 summarize the percentages of different AODE and AODC values for BDS satellites over the analysis period. The results suggest a noticeable difference between the values of AODC and AODE. This is caused by the fact that the generation of clock information is separate from the orbit determination process (Wu et al., 2017). The data also reveal that the BDS-2 MEOs have the longest AODs due to the limited ground tracking and uploading stations. As for BDS-3, the AODs are mostly shorter than an hour, which highlights the benefits of the ISLs.

URA Index (URAI) is broadcast as an indicator of URA, which provides a conservative RMS estimate of the SIS-induced pseudorange errors. A part of the relationship between URAI and URA is briefly shown as

**TABLE 1** Calculation of time group delay corrections (J. Guo, personal communication, August 1, 2020)

Organization	Time span	Reference point	Correction
GFZ	All	B1I+B2I IF	$T_{GD}^i = \frac{f_{B1}^2}{f_{B1}^2 - f_{B2}^2} T_{GD1}^i - \frac{f_{B2}^2}{f_{B1}^2 - f_{B2}^2} T_{GD2}^i$
WHU	Until DOY 365, 2018	B1I+B2I IF	
	Since DOY 001, 2019	B1I+B3I IF	$T_{GD}^i = \frac{f_{B1}^2}{f_{B1}^2 - f_{B3}^2} T_{GD1}^i$

Note:  $f_{B1}^2$ ,  $f_{B2}^2$ , and  $f_{B3}^2$  are the frequencies of B1I, B2I, and B3I, respectively.

**TABLE 2** The distribution of the AODE value (unit: Hours) for BDS satellites

Satellite type	AODE (%)			
	$\leq 1$	(1, 6]	(6, 24]	$> 24$
GEO	99.91	0.09	0.00	0.00
IGSO	84.00	15.70	0.30	0.00
MEO	38.10	25.01	36.65	0.24
BDS-3	95.77	3.65	0.52	0.06

**TABLE 3** The distribution of the AODC value (unit: Hours) for BDS satellites

Satellite type	AODC (%)			
	$\leq 1$	(1, 6]	(6, 24]	$> 24$
GEO	98.61	1.33	0.06	0.00
IGSO	74.91	24.15	0.94	0.00
MEO	20.49	24.13	54.55	0.83
BDS-3	96.35	3.11	0.54	0.00

follows, and the full version is given in the interface control document (ICD) (CSNO, 2019a):  $URAI = 0$ ,  $0.00 \text{ m} < URA \leq 2.40 \text{ m}$ ;  $URAI = 1$ ,  $2.40 \text{ m} < URA \leq 3.40 \text{ m}$ ;  $URAI = 2$ ,  $3.40 \text{ m} < URA \leq 4.85 \text{ m}$ ;  $URAI > 2$ ,  $URA > 4.85 \text{ m}$ . Table 4 shows that the URAI value is nearly always equal to two, i.e., the broadcast URA is usually bounded by 4.85 meters.

For safety purposes, the broadcast ephemeris indicates the health status of a satellite using the health flag. When this flag is set to “1,” the associated satellite is deemed as unhealthy and encounters an outage. Table 5 shows the percentages of unhealthy ephemerides for different types of satellites. The results indicate that the BDS-2 MEOs are most frequently subject to failures.

**TABLE 4** The distribution of the URAI value for BDS satellites

Satellite type	URAI (%)			
	0	1	2	$> 2$
GEO	2.22	0.00	97.78	0.00
IGSO	0.92	0.00	99.08	0.00
MEO	0.09	0.00	99.91	0.00
BDS-3	0.08	0.00	99.92	0.00

**TABLE 5** Percentages of unhealthy ephemerides for BDS satellites

Satellite type	GEO	IGSO	MEO	BDS-3
Frequency (%)	1.30	0.63	3.16	0.61

In this work, we perform the SIS performance evaluation with all healthy ephemerides, without partitioning the data by AODC, AODE, and URAI. Therefore, we can obtain a unique overbounding URA for each satellite, which can cover all nominal situations. However, it should be noted that this may lead to optimistic estimates for some AOD values because the SIS accuracy might vary as a function of AODs. Appendix B provides a quantitative analysis on this relationship, and the results suggest that the variation in accuracy with AODs is considerable for a few BDS-2 satellites (mainly the MEOs) but not very obvious for the others. The analysis also reveals that the partition by AODs may fail because the samples at some AODs are not sufficient to be statistically meaningful.

## 2.4 | Signal-in-space range error (SISRE) computation

Signal-in-space error (SISE) is one of the major pseudorange error budgets. It is usually approximated as the orbital error vector  $[\Delta e_R \ \Delta e_A \ \Delta e_C]^T$  in the local orbital frame and the clock error term  $\Delta T$ . In this work, other small contributors to the SISRE are ignored, e.g., antenna bias and signal deformation, but their effects will be considered in future work. The radial (R), along-track (A), and cross-track (C) orbital errors are computed as

$$[\Delta e_R \ \Delta e_A \ \Delta e_C]^T = A_E^O \cdot [\Delta x \ \Delta y \ \Delta z]^T, \quad (4)$$

where  $[\Delta x \ \Delta y \ \Delta z]^T$  is the ECEF orbital error vector and  $A_E^O$  denotes the transformation matrix from ECEF to the local orbital frame. For a given satellite position  $\mathbf{r}$  and an inertial velocity  $\mathbf{v}$  in ECEF, the transformation matrix is determined as (Montenbruck, Schmid, et al., 2015)

$$A_E^O = \begin{bmatrix} \frac{\mathbf{r}}{|\mathbf{r}|} & \frac{\mathbf{r} \times \mathbf{v}}{|\mathbf{r} \times \mathbf{v}|} \times \frac{\mathbf{r}}{|\mathbf{r}|} & \frac{\mathbf{r} \times \mathbf{v}}{|\mathbf{r} \times \mathbf{v}|} \end{bmatrix}^T. \quad (5)$$

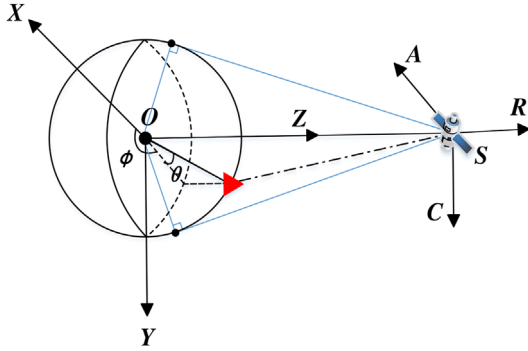


**FIGURE 5** Geometric method to calculate the IURE [Color figure can be viewed in the online issue, which is available at [wileyonlinelibrary.com](http://wileyonlinelibrary.com) and [www.ion.org](http://www.ion.org)]

To reveal the effect of SISEs on a navigation user, SIS [user] range error (SISRE or SIS URE) is calculated by projecting the SISE into the user line-of-sight (LOS) direction. And instantaneous URE (IURE) represents the equivalent pseudorange error (i.e., SIS URE) at a given epoch. Figure 5 gives a graphical illustration of the IURE calculation. As shown in this figure, we adopt a geocentric frame (O-XYZ), which is aligned with the axes of the local orbital frame (S-RAC). Therefore, with respect to ECEF, the O-XYZ frame varies with satellite motion. For a user at a distance  $d$  from the Earth's center, the IURE is computed as (Wu et al., 2017)

$$IURE = -\frac{[\Delta e_R \quad \Delta e_A \quad \Delta e_C]}{\sqrt{1 + \kappa^2 - 2\kappa \sin(\theta)}} \begin{bmatrix} \kappa - \sin(\theta) \\ \cos(\theta) \cos(\phi) \\ \cos(\theta) \sin(\phi) \end{bmatrix} + \Delta T, \quad (6)$$

where the user location is determined by the latitude  $\theta$  (above the xy-plane), the longitude  $\phi$  (measured relative to the x-axis in the xy-plane), and the distance  $d$ ;  $\kappa = |\mathbf{r}|/d$  denotes the normalized distance between the satellite and the geocenter. If the receiver mask angle is zero, the minimum latitude  $\theta_{\min}$  of the satellite's coverage footprint is computed as  $\theta_{\min} = \sin^{-1}(1/\kappa)$ . As a reminder,  $\theta$  and  $\phi$  are calculated in the O-XYZ frame rather than ECEF.

To capture the IURE variation over user locations, there have been some commonly used metrics for global SIS URE statistical description, e.g., global-average URE, worst-case URE (or maximum projected error, MPE), and user projected error (UPE). Their definitions are illustrated in detail as follows.

Global-average URE describes the average URE over the Earth's surface within the satellite's coverage (Wu et al., 2017). It has been widely used in various GNSS performance standards, e.g., GPS positioning service performance standard (DoD, 2008). However, this criterion is not

acceptable in safety-critical applications because it cannot safely bound the errors in all possible situations.

Worst-case URE, also called MPE, represents the maximum IURE for a user in the satellite's footprint at a particular time (Walter et al., 2018). This indicator is often employed in the evaluation of SIS integrity performance (Wu et al., 2017). However, it is not well suited for determining the overbounding URA. This is because, first, it could lead to an overly conservative estimate due to the impossible assumption that the user always experiences the maximum IURE. Second, the MPE distribution will not be Gaussian even if all the underlying distributions of orbit and clock errors are Gaussian. More specifically, this distribution is bimodal with a notch at zero (Walter et al., 2018).

UPE is the satellite orbit and clock error projected onto a specific time-invariant user location (Walter et al., 2018). A large number of globally distributed users are selected for calculating the UPEs. Each healthy satellite is visible to many but not all users at any given epoch. Therefore, unlike MPE, there will be multiple UPE values per satellite at each epoch (one for each user that has this satellite in view).

Aside from the metrics above, this paper proposes a new metric, user-grid URE, for characterizing the SISREs. As shown in Figure 5, the location of a user is specified by a pair of latitude  $\theta$  and longitude  $\phi$ , and the coverage area of a satellite is described as  $\theta_{\min} \leq \theta \leq 90^\circ$  &  $0^\circ \leq \phi < 360^\circ$ . We select a mesh of users evenly distributed in this area such that they provide a sufficient coverage density. The user-grid URE of a satellite is obtained by calculating the IUREs for each user. Similar to UPE, there will be multiple user-grid URE values per satellite at each epoch. The major difference between the two metrics is the user selection strategy. In the UPE approach, the users are fixed on the Earth's surface, and the normalized user-satellite (i.e., LOS) vector varies with satellite motion. In contrast, user-grid URE keeps the LOS vector invariant for each user by changing their locations in the ECEF frame.

In this study, we use user-grid URE to evaluate the nominal SISRE performance and to determine the overbounding URA for each monitored satellite. This metric can provide a safe estimate because it covers every possible situation that a user may encounter, including the worst condition. Compared to MPE, this metric offers a significant advantage: the error distribution of every user will be Gaussian if the orbit and clock errors have Gaussian distributions. This can be proved by Equation (6): the IURE of a user is a linear time-invariant combination of these error components. It also shows an advantage over UPE: because the analyzed satellite is always visible to every selected user, the number of samples associated with each user is exactly equal to the number of valid epochs. A disadvantage of user-grid URE is its inconvenience in



evaluating the SISREs in a chi-square form (Walter et al., 2018), but this is beyond the scope of this work.

### 3 | ANOMALIES: DETECTION AND PROBABILITY DETERMINATION

#### 3.1 | Definitions of SIS faults

SIS anomalies (i.e., faults) are mainly caused by incorrect navigation data, orbital maneuvers, abnormal orbital disturbances, clock jumps, clock drifts, and other unusual events (Gunning et al., 2018). SIS faults can potentially lead to large navigation errors and constitute the major threats to navigation safety in aviation applications.

In this study, we adopt two different definitions of SIS faults and term them as Definition a and Definition b, respectively. The former is a new definition that takes the fault shape into consideration, and the latter is a snapshot approach recommended by Walter et al. (2019). Both definitions depend on a predefined threshold, and the rationale of the threshold determination is given as follows. In prior studies, the threshold is usually given as  $4.42 \times \bar{\sigma}_{\text{URA}}$ , where  $\bar{\sigma}_{\text{URA}}$  denotes the broadcast URA (Walter et al., 2019). However, we advocate selecting a set of thresholds for the following reasons: first, we are not sure whether the broadcast URA can properly describe the true error distributions; second, this threshold is an important parameter that significantly influences the estimated URA and fault probability; third, this approach can offer a more comprehensive characterization of the SISREs than solely adopting one threshold.

The two definitions are illustrated in detail as follows. Under Definition a, an SIS fault is defined as an event occurring when there is an abnormal value or trend in the SIS UREs. The abnormal value refers to the IURE whose magnitude exceeds the threshold. And an abnormal trend is said to exist when (a) the IURE data at several consecutive epochs form a curve with a ramp, sinusoidal, or any nonrandom shape, and (b) this curve contains at least one abnormal value. Under Definition b, an SIS fault is defined to occur whenever the IURE is greater than the threshold (Walter et al., 2019).

Figure 6 shows the difference between the two definitions by simulating a ramp fault. This figure shows that the fault duration is different under these two definitions. At the beginning of this fault, the URE magnitudes are below the threshold, but there is clearly an abnormal trend. These samples are regarded as faulted under Definition a, while they are considered unfaulted under Definition b. Therefore, the fault duration is extended under Definition a, and thus, the fault probability is increased, which is the trade-off for potentially reducing the URA.

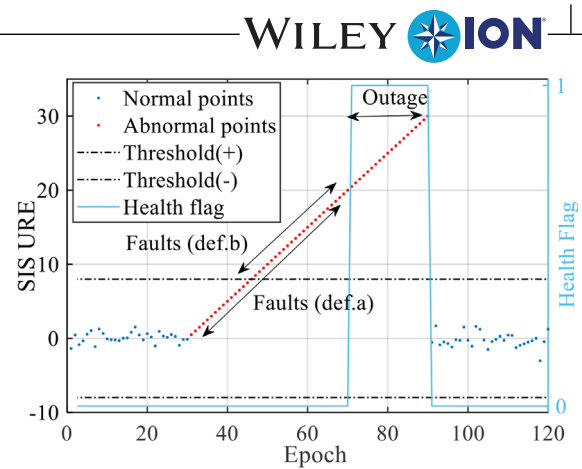


**FIGURE 6** Graphical illustration of the SIS fault definitions [Color figure can be viewed in the online issue, which is available at [wileyonlinelibrary.com](http://wileyonlinelibrary.com) and [www.ion.org](http://www.ion.org)]

Prior studies usually adopt Definition b because (a) it avoids any ambiguity about whether a fault exists and maintains consistency with GPS performance standards and (b) the below-threshold segment imposes little threat to the users. However, the new definition is also reasonable and meaningful, although it is somewhat ambiguous. This is because, first, it is safe (i.e., conservative) to regard a sample as faulted in the determination of ISM parameters. This is actually a trade-off between URA and fault probability. Second, as an alternative, this definition can broaden the understanding of the distinction between “faulted” and “nominal” samples, which will be further illustrated in Section 4.2.

#### 3.2 | Anomaly detection

This section presents how to detect the anomalies in the observed data. The worst-case URE (MPE) metric is employed in this task because the most vulnerable user must be protected in integrity-related applications (Walter & Blanch, 2015). It is straightforward to implement anomaly detection under Definition b (Walter et al., 2019). However, it is hard to unambiguously perform this task under Definition a due to the difficulty in accurately identifying all the samples that belong to a fault. In this paper, we present a simple and empirical scheme to roughly estimate the start and end time of a fault as follows. This scheme is preliminary and should be viewed as an example. And due to the manual operation in the final step, it cannot automate in an ISM generator (ISMG). In future work, it will be improved to support autonomous and reliable anomaly detection.

1. Detect the faults based on Definition b, and record the faulted epochs.

2. If a fault lasts over 45 minutes (changeable) and its first or last data differs from the threshold by less than 10 meters (changeable), go to step (3); otherwise, this fault is regarded as an outlier or a step fault.
3. Plot the curve of this fault with the surrounding data, and manually estimate its start and end epochs based on the curve.

### 3.3 | Determination of fault probabilities

Walter et al. (2019) have presented the precise definitions of prior fault probabilities and have used them for the assessments of GPS and GLONSS. These definitions are also adopted in this study, and they are briefly illustrated as follows.

According to the ARAIM baseline algorithm, we consider two nonoverlapping classes of SIS fault probability that account for satellite faults and constellation faults, respectively. The probability of satellite fault,  $P_{\text{sat}}$ , is defined as the probability that an individual satellite is in a fault state at any given time. And the probability of constellation fault,  $P_{\text{const}}$ , is the probability that multiple satellites in a constellation are simultaneously faulted due to a common cause.

Fault rate  $R$  is defined as the probability that a healthy satellite or constellation becomes faulted within a period of time. Let  $N_F$  be the number of fault occurrences within a total time interval  $T_t$ , evaluating  $R$  is equivalent to deriving the expected value of  $R$  given  $N_F$  and  $T_t$ , i.e.,  $E(RN_F)$ . Rigorous derivations have been established by Walter et al. (2019) with key assumptions laid out and all the steps carefully justified. They examined *a priori* probabilities of  $R$  that are proportional to  $R^m$ , where  $m$  is an exponent. Based on this, the final estimate of  $R$  ( $\hat{R}$ ) is (Walter et al., 2019)

$$\hat{R} = E(RN_F) = \frac{N_F + m + 1}{T_t} = \frac{N_F + 1/2}{T_t}. \quad (7)$$

This equation applies  $m = -1/2$  in the final term, and the justifications for this choice are provided by Walter et al. (2019). In brief, the choice of  $m = -1/2$  ensures that the evaluation results are consistent across different parameterizations (i.e., fault rate,  $R$ , versus mean time between faults,  $1/R$ ). In this paper, we will directly employ Equation (7) for fault rate evaluation, although this is not the unique approach to do this.

Fault probability  $P$  is related to fault rate  $R$  through the following equation:

$$P = MTTN \times R. \quad (8)$$

MTTN denotes the expected average fault duration. A fault is said to be over when it is corrected or the

user is notified by the broadcast ephemeris. MTTN is an important indicator that shows the control segment's ability to monitor and repair SIS faults. Since CSNO has not yet provided any commitment on this parameter, in this work, we preliminarily estimate the MTTN values based on the historical observations.

## 4 | NOMINAL PERFORMANCE: SIS URE ANALYSIS METHODOLOGY

### 4.1 | Unfaulted SIS UREs and URA definition

Section 4 focuses on evaluating the nominal SIS performance with unfaulted SIS UREs. If an IURE is not identified as a fault, then it is under nominal conditions. Therefore, the evaluation will be directly affected by the fault definition and the threshold. This evaluation aims at properly estimating the URA values for each monitored satellite. URA provides a conservative estimate (i.e., an integrity overbound) of the uncertainty on the SIS URE (Walter, Blanch, & Gunning, 2019). Although this parameter is available in the navigation message, it must be validated or adjusted (if necessary) by air navigation service providers (ANSP) before being provided to aviation users. For this purpose, Section 4.2 presents the methodology to estimate a safety-assured URA based on the observed data.

### 4.2 | Overbounding SIS UREs

In ARAIM algorithms, range errors are usually described by Gaussian models. However, the actual error distributions are usually not ideally Gaussian due to complex disturbances (Walter et al., 2018). Fortunately, various overbounding techniques have been proposed to derive a conservative Gaussian distribution with the observed one. The definition of overbounding can be mathematically described as follows (Larson, 2018):

$$\begin{aligned} P(X_{\text{ob}} \leq x) &\geq P(X \leq x), \forall x < \bar{x} \\ P(X_{\text{ob}} \leq x) &\leq P(X \leq x), \forall x > \bar{x} \end{aligned} \quad (9)$$

where  $P$  denotes the probability of the event inside the parentheses,  $X_{\text{ob}}$  is the random variable of the overbounding distribution,  $X$  is the random variable of the actual distribution, and  $\bar{x}$  is the error-free value of  $X$ . Equation (9) is an expression in the form of a cumulative distribution function (CDF). In GNSS integrity domain, single-CDF overbounding (DeCleene, 2000), paired-CDF overbounding (Rife, Pullen, Enge, & Pervan, 2006; Rife, Walter, & Blanch, 2004), two-step overbounding

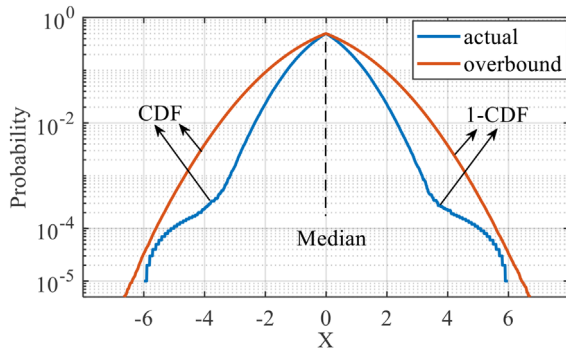


**FIGURE 7** Graphical depiction of the FCDF overbounding concept [Color figure can be viewed in the online issue, which is available at [wileyonlinelibrary.com](http://wileyonlinelibrary.com) and [www.ion.org](http://www.ion.org)]

(Blanch, Walter, & Enge, 2018), and three-condition overbounding (Martini et al., 2020a) are four Gaussian overbounding approaches. A peculiar single-CDF approach, called folded CDF (FCDF), is adopted in this work. In this approach,  $\bar{x}$  is equal to the median of  $x$ , and thus,  $P(X \leq \bar{x}) = 0.5$  (Larson, 2018).

It is acceptable to use a single-CDF approach for the analysis, although the other three approaches show advantages in (a) avoiding the requirements on symmetry and unimodality and (b) ensuring the conservativeness after convolution. This is because, first, the overbounding results might be excessively conservative when applying the latter three approaches (Walter et al., 2018). Second, Appendix C shows that for most of the satellites, the orbit and clock errors approximately conform to symmetric and unimodal distributions. Moreover, prior studies on GPS have examined that the range errors do not convolve in a hazardous way before the position error exceeds the protection level (Walter et al., 2018). In future work, we will analyze the effect of error convolutions in BDS and will also consider the three advanced approaches for more reliable evaluations.

Figure 7 provides a graphical depiction of the FCDF overbounding approach. In this figure, the actual heavy-tailed distribution is simulated by mixing 40 points uniformly distributed in  $(-6, -4] \cup [4, 6)$  with  $10^5$  points from the Gaussian distribution  $\mathcal{N}(0, 1^2)$ , and the overbounding distribution is  $\mathcal{N}(0, 1.5^2)$ . This figure indicates that merely overbounding the core distribution may lead to an overly optimistic estimate, and it also suggests that the beginning segment of a ramp fault is a possible cause of heavy tails.

As mentioned in Section 2.4, the user-grid URE metric is used to evaluate the nominal SIS performance. To conduct the evaluation for a satellite, we first select a mesh of users that are evenly distributed in its coverage footprint. For BDS, the orbit altitude is 35,786 kilometers for the GEOs and IGSOs and 21,528 kilometers for the MEOs (CSNO, 2019a). Therefore, if the user is near the Earth's

**TABLE 6** Latitude ( $\theta$ ) and longitude ( $\phi$ ) grids for generating a mesh of users

	$\theta$ grid ( $^\circ$ )	8.73	10	15	...	90
GEO/IGSO	$\phi$ grid ( $^\circ$ )	0	10	20	...	350
MEO	$\theta$ grid ( $^\circ$ )	13.18	15	20	...	90
	$\phi$ grid ( $^\circ$ )	0	10	20	...	350

surface and its mask angle is zero, the minimum latitude  $\theta_{\min}$  is  $8.73^\circ$  for the GEO/IGSO satellites and  $13.18^\circ$  for the MEO satellites. Table 6 gives the locations of the selected users with respect to the O-XYZ frame shown in Figure 5. These users are fixed in this frame to keep their LOS vectors toward the analyzed satellite invariant with time. As a reminder, the definitions of latitude and longitude here are different from those in the geographic coordinate systems (e.g., WGS84).

Finally, the following steps show how to determine the overbounding URA ( $\sigma_{\text{URA}}$ ) for a satellite.

1. Calculate the IUREs for every selected user at each epoch when there are both healthy BCE and valid PCE.
2. Perform anomaly detection by comparing the MPES with the threshold; then, if epoch  $i$  is labeled as “faulted,” change all the IUREs of this epoch to  $\infty \times \text{sign}(\text{MPE}[i])$ .
3. Form the IURE time series for each user so that we can evaluate the IURE distributions for each user separately.
4. For each user, (a) estimate the mean of the corresponding IURE time series, (b) remove this value to form the zero-mean IURE distribution, and (c) generate an FCDF curve based on this IURE distribution.
5. Find a Gaussian distribution  $\mathcal{N}(0, \sigma_{\text{URA}}^2)$  that can strictly overbound the FCDF curves of ALL users for  $\forall \text{IURE} \in [-T_l, T_r]$ , where  $T_l = \min\{\text{IURE} \mid \text{IURE} < 0 \text{ and IURE is finite}\}$  and  $T_r = \max\{\text{IURE} \mid \text{IURE} > 0 \text{ and IURE is finite}\}$ .

Figure 8 provides the overbounding results of C09 to further illustrate the method above. In this figure, each colored thin line represents the IURE distribution of a user, and the heavy blue line denotes the overbounding Gaussian distribution. Under the 10-meter threshold, the number of faulted samples is 86 under Definition a and 41 under Definition b. As a trade-off, the nominal distributions that are to be bounded for evaluating the URA are obviously less heavy-tailed under the former definition as compared to the latter one. Specifically,  $|T_l|$  and  $T_r$  are about 8 meters under Definition a and 10 meters under Definition b. This results in a smaller overbounding URA under the former definition at the cost of an increase in fault probability. The trade-off shown here proves

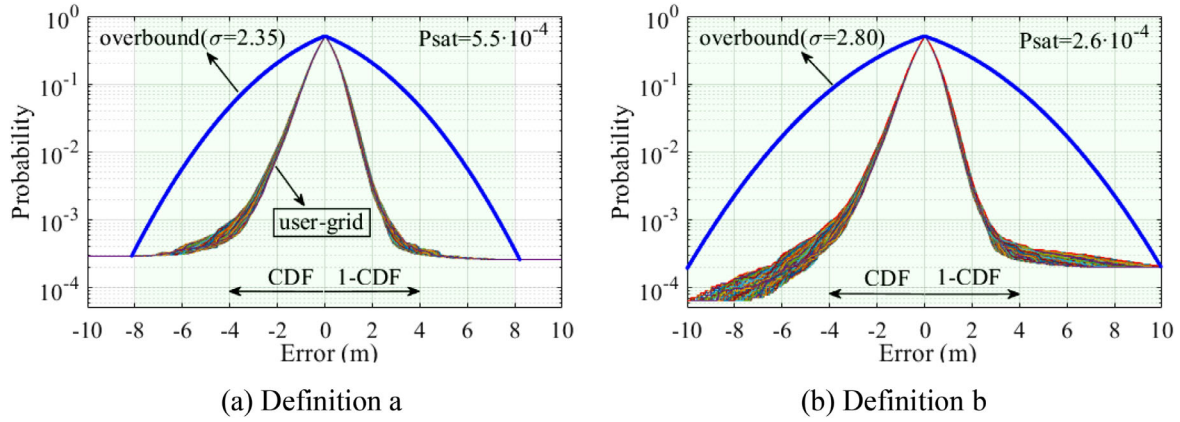


FIGURE 8 Bounding the user-grid UREs for C09 under different fault definitions, where the green shadow indicates the “nominal” distribution to be bounded [Color figure can be viewed in the online issue, which is available at [wileyonlinelibrary.com](http://wileyonlinelibrary.com) and [www.ion.org](http://www.ion.org)]

the significances of the new definition (Definition a): it broadens the understanding of SIS faults and serves as a supplement to the original definition (Definition b).

## 5 | BDS SISRE BEHAVIORS AND DISCUSSIONS

### 5.1 | Example analysis

Based on the proposed SISRE evaluation scheme, this subsection shows some results as the examples to further illustrate the associated methods and to identify some special BDS SIS features. This part is a complement to the results in Section 5.2 where we quantitatively evaluate the integrity performance of every monitored satellite.

First, Figure 9 compares the error behaviors among different types of satellites. In this figure, the error distributions are formed without removing any sample. And to allow for a clearer view, the x-axis is limited to  $\pm 30$  meters and the y-axis ranges from  $10^{-5}$  to 1. Note that, the errors of C21 are all smaller than 8 meters. This figure proves the superior SIS accuracy of BDS-3 as compared to BDS-2. And it also shows that these error distributions (except MPE) appear to have a Gaussian core while their tail data seem to have a larger variance than the majority. This is clear evidence of the occurrence of heavy tails, and this phenomenon is also reported in GPS and other constellations (Walter et al., 2018).

Figure 10 shows the profiles of several SIS fault types observed in the dataset. The shape of a fault is related to its underlying causes. And the causes can be identified by analyzing the surrounding broadcast parameters. For example, the ramp fault in this figure was caused by clock instability, and the sinusoidal fault was due to incorrect orbit parameters (specifically, the rate of right ascension  $\dot{\Omega}$

and the sine harmonic correction term to inclination angle  $C_{is}$  were incorrect).

Next, we use an example of an SIS fault occurring in an MEO to illustrate how a fault is corrected in orbit. Figure 11 presents the orbit and clock errors over the corresponding period, and Table 7 gives the broadcast navigation parameters. As seen, this is a ramp clock fault whose magnitude increases from a small value to 60 meters. And the table indicates that this fault was caused by incorrect clock parameters. This fault had lasted 18 hours before the user was notified by a new navigation message (the fourth row in Table 7), where the health flag was set to one. Note that, the clock correction parameters were not updated in this message, and thus, the AODC was unchanged. The reason behind the long fault duration is the limited distribution of BDS-2's ground tracking and uploading stations (Wu et al., 2017). Finally, Table 7 shows that the satellite recovered from the fault after the new clock parameters were uploaded to the satellite and broadcast to the users.

Special attention should be paid to the anomalous SIS performance evaluation for BDS-2 MEOs. Since BDS-2 only serves the Asia-Pacific region ( $55^{\circ}\text{S}\sim 55^{\circ}\text{N}$ ,  $70^{\circ}\text{E}\sim 150^{\circ}\text{E}$ ), it is reasonable to remove the faulted data that do not affect any user in this region from the evaluation. And in safety-critical applications, it is strongly suggested that the ARAIM software and/or the receiver disable the BDS-2 satellites when the user is outside this region. Figure 12 summarizes all the faulted data of C11 (45 faults in total) and shows the corresponding subsatellite points. There is a green curve in this figure, and the area inside this curve is called the “dark zone.” When an MEO flies over this zone, it is completely invisible to all the users in the BDS-2's service region (the user mask angle is  $15^{\circ}$ ). This figure indicates that many faulted data correspond to this zone and they should be removed from the determination of fault probability, fault rate, and MTTN.



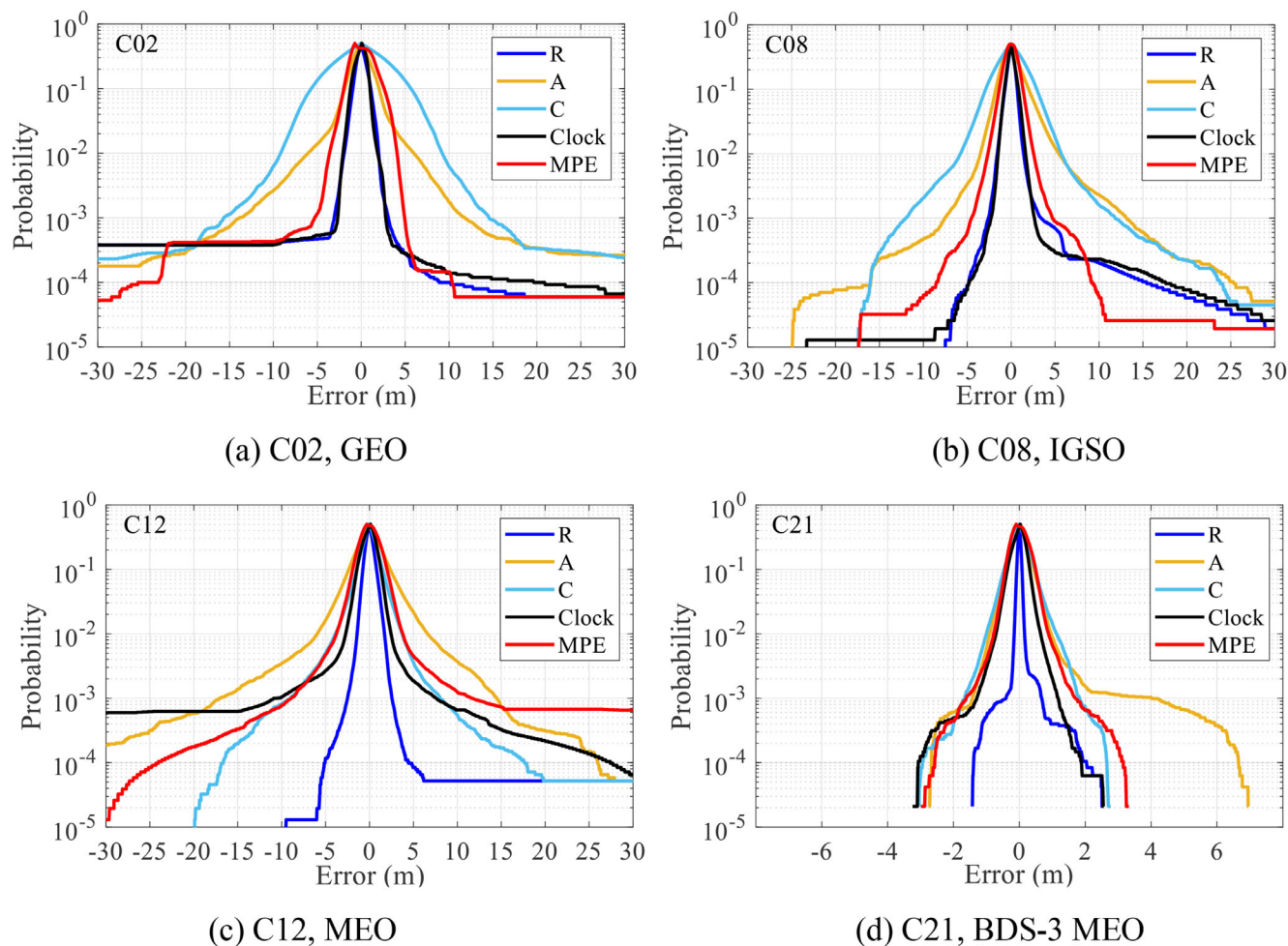


**FIGURE 9** Radial (R), along-track (a), cross-track (c), clock, and the maximum projected error distributions in the form of FCDF for various satellites [Color figure can be viewed in the online issue, which is available at [wileyonlinelibrary.com](http://wileyonlinelibrary.com) and [www.ion.org](http://www.ion.org)]

**TABLE 7** Broadcast clock parameters (C11, brdm2010.17n)

toc	tom	Clock bias (s)	Clock drift (s/s)	Clock drift rate (s/s <sup>2</sup> )	Health	AODC
05:00:00	05:00:00	1.270088832825e-04	-1.672262328611e-11	-1.387778780781e-17	0	18
06:00:00	06:00:00	1.269486965612e-04	-1.693312157158e-11	-1.387778780781e-17	0	19
06:00:00	06:02:30	1.269486965612e-04	-1.693312157158e-11	-1.387778780781e-17	1	19
07:00:00	07:00:00	1.270910724998e-04	-1.157740570079e-11	0.000000000000e+00	1	0
07:00:00	07:02:00	1.270910724998e-04	-1.157740570079e-11	0.000000000000e+00	0	0

## 5.2 | Preliminary estimates of URA and fault probability for BDS satellites

This section presents detailed BDS SISRE characteristics and compares the SIS performance among different satellites. First, we provide the estimated values of URA and fault probability for each satellite as follows. In the evaluation, Definition b is adopted as the primary definition while Definition a is only applied to some satellites where the two definitions can lead to significantly different esti-

mates of URA. Please note, the following results can only be viewed as preliminary due to (a) the relatively frequent absence of PCEs and BCEs and (b) the limited data volume.

Figures 13–15 present the estimated values of URA ( $\sigma_{\text{URA}}$ ) and fault probability for various types of BDS-2 satellites. We can draw the following conclusions from the results. First, as the detection threshold is raised,  $\sigma_{\text{URA}}$  tends to increase while the fault probability will decrease. Their values will probably level off if the threshold is large enough. Besides, for some satellites (e.g., C09–C11),  $\sigma_{\text{URA}}$

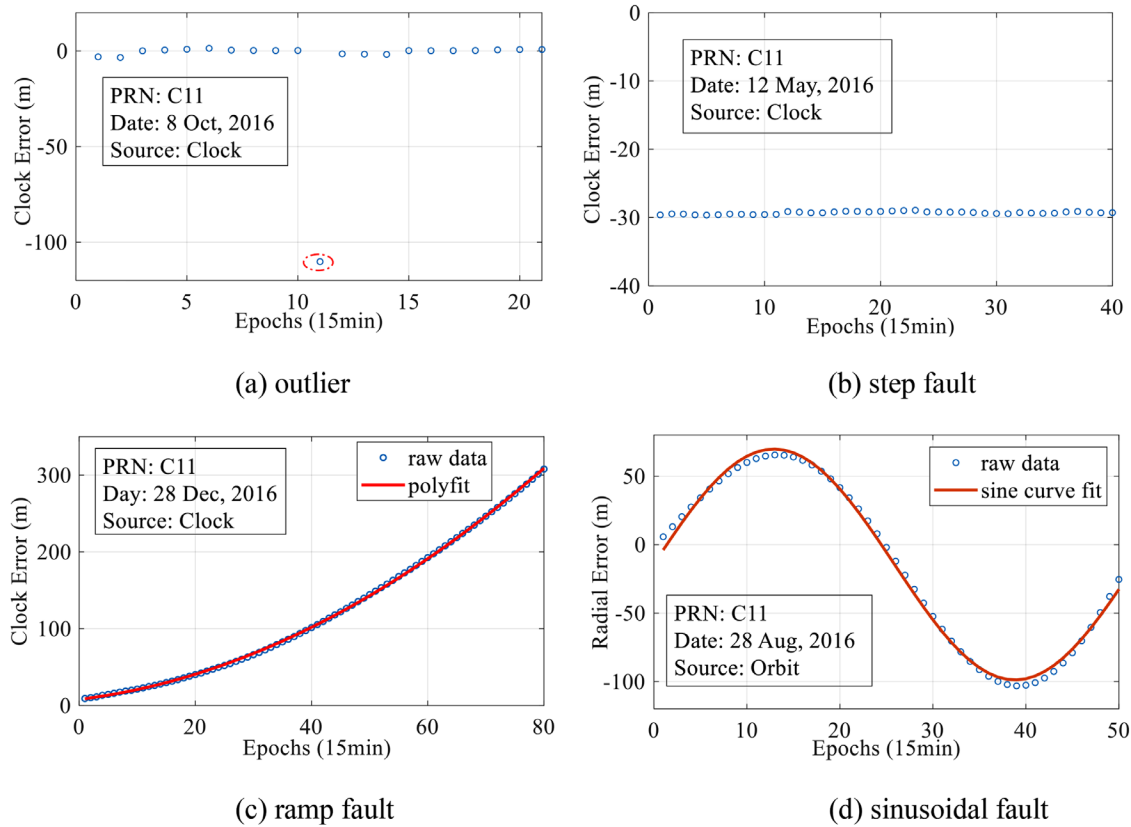


**FIGURE 10** The profiles of various types of SIS faults observed in the dataset [Color figure can be viewed in the online issue, which is available at [wileyonlinelibrary.com](http://wileyonlinelibrary.com) and [www.ion.org](http://www.ion.org)]

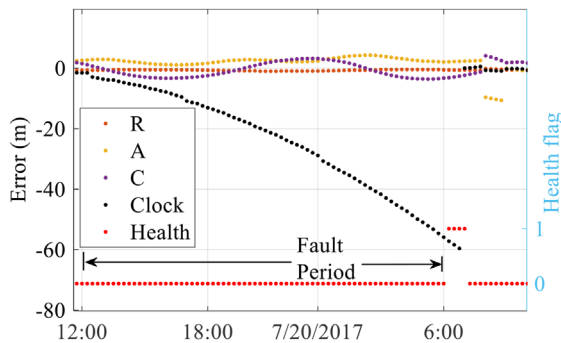


**FIGURE 11** Orbit and clock errors when a fault occurs in C11 (MEO) [Color figure can be viewed in the online issue, which is available at [wileyonlinelibrary.com](http://wileyonlinelibrary.com) and [www.ion.org](http://www.ion.org)]

differs significantly under different fault definitions. This implies that the tail error distributions of these satellites are greatly impacted by ramp faults. Similarly, Figure 16 shows the results for the monitored BDS-3 satellites. It is obvious that the conclusions above are also valid for BDS-3. Please note, these figures demonstrate the variation in the results with fault definitions and thresholds, but we do not know which set of results can best describe the long-

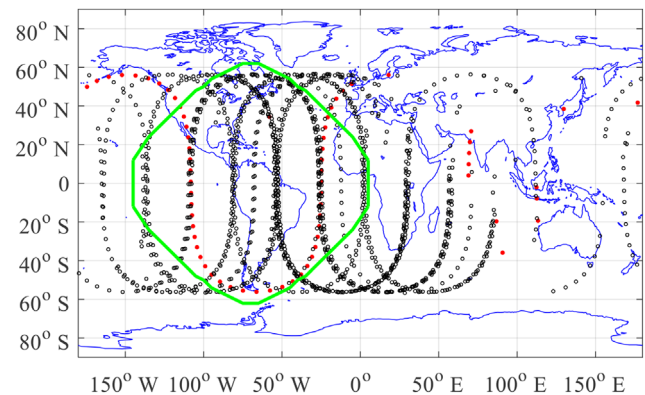


**FIGURE 12** Subsatellite points of C11 when it is under faulted conditions, where black indicates clock faults, red denotes orbit faults, and the green curve shows the dark zone [Color figure can be viewed in the online issue, which is available at [wileyonlinelibrary.com](http://wileyonlinelibrary.com) and [www.ion.org](http://www.ion.org)]

term planned behaviors. This remains an open problem for future investigations.

Then, we further compare the SIS performance among different satellites as follows. Hereafter, the threshold is set to 10 meters for BDS-2 satellites and 4 meters for BDS-3 satellites. Please note, although Table 4 offers the

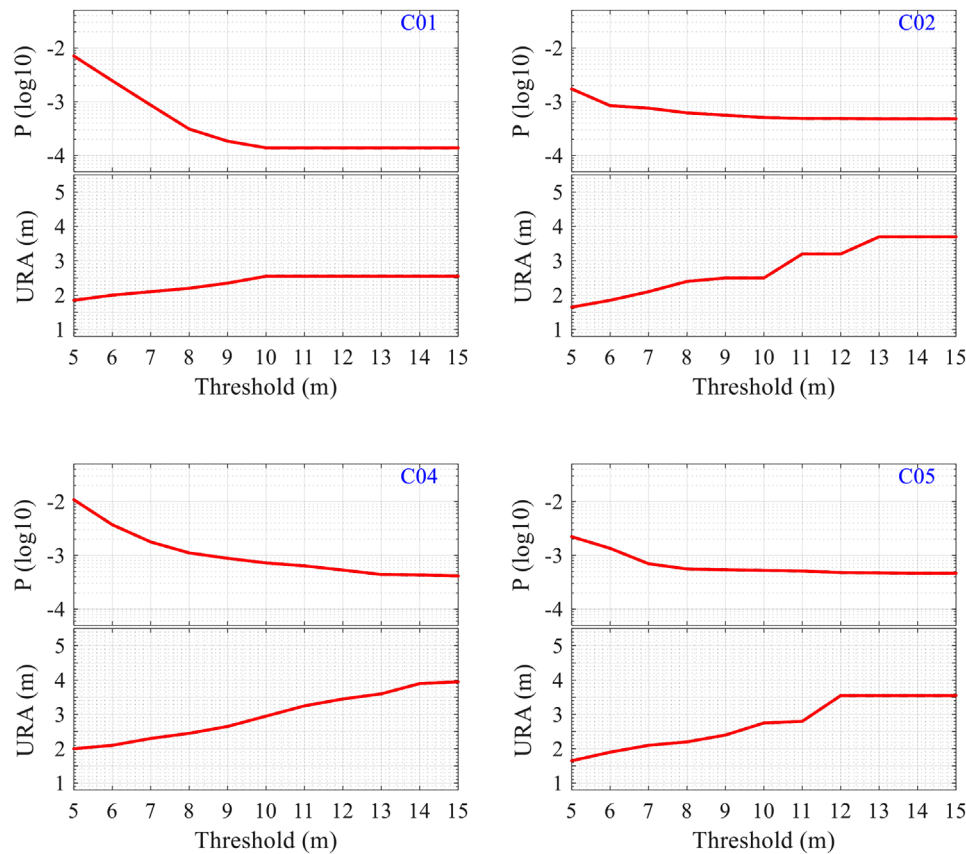


**FIGURE 13** The estimated values of URA and fault probability ( $P$ ) for BDS-2 GEO satellites under Definition b [Color figure can be viewed in the online issue, which is available at [wileyonlinelibrary.com](http://wileyonlinelibrary.com) and [www.ion.org](http://www.ion.org)]

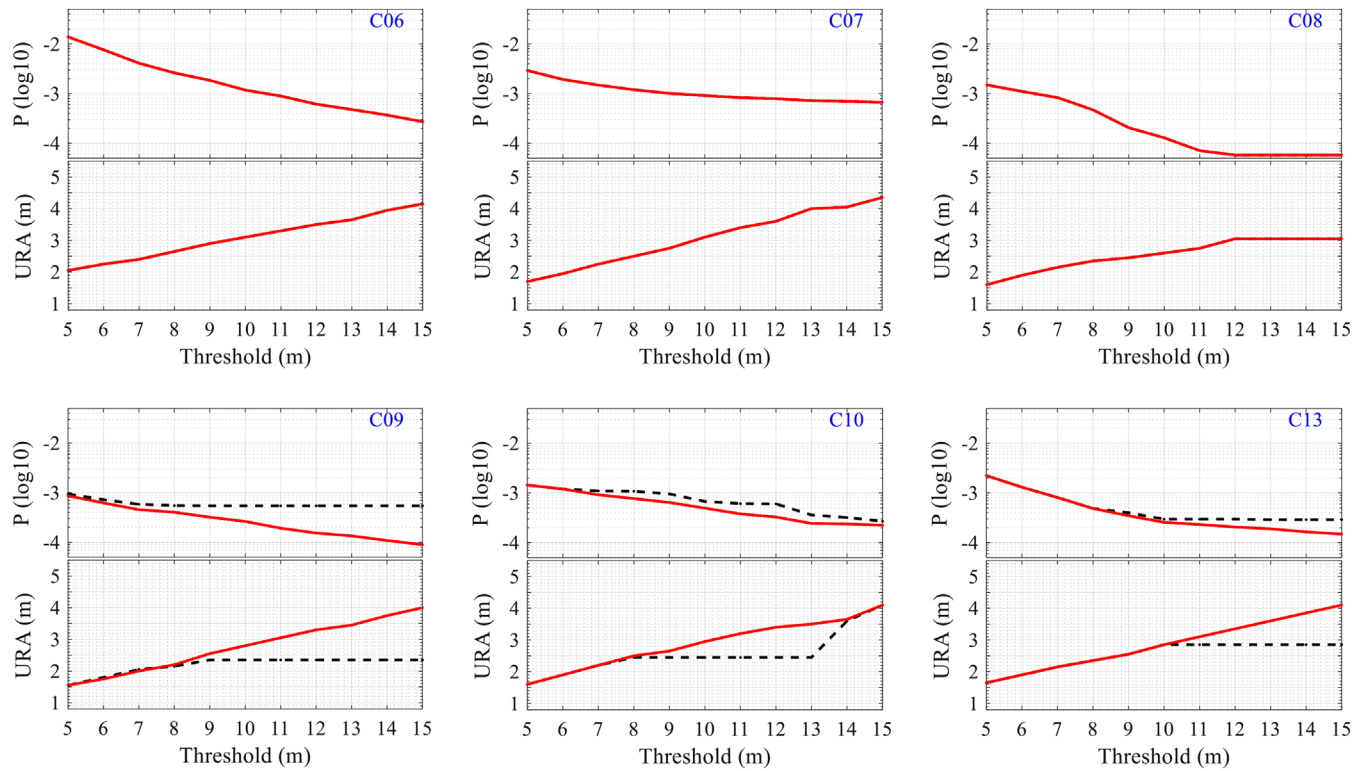
broadcast URAs, we do not choose the thresholds based on them because we are not confident that (a) they can accurately describe the actual SISRE behaviors (the results above show that they might be overly conservative), and (b) the Constellation Service Provider (CSP) will make the commitments based on them (because the CSP may make commitments in written specifications, e.g., Open Service Performance Standard). Figures 9 and A8-A9 (Appendix C) demonstrate that for most BDS-2 satellites, the UREs are mostly below 10 meters and almost all the UREs above this number correspond to some fault events (e.g., ramp faults). This conclusion is also true for BDS-3 satellites when the threshold is 4 meters. Therefore, it is initially acceptable to use these two thresholds for the preliminary performance evaluation and comparison.

Figure 17 presents the estimated URAs ( $\sigma_{\text{URA}}$ ) for all the monitored satellites, and Figure 18 shows the corresponding fault probabilities. The results suggest that most of the BDS-2 satellites hold the  $\sigma_{\text{URA}}$  of 2.4~3.2 meters, except C11 whose  $\sigma_{\text{URA}}$  is greater than 3.4 meters. Their fault probabilities also vary a lot with a range from  $1.5 \times 10^{-4}$  (C01 and C08) to  $4.5 \times 10^{-3}$  (C11). Please note, these results are derived under the assumption that there is no fault during any of the data outages. Given the large variability in

performance over satellites, it is strongly suggested to set different values for individual satellites in the ISM rather than merge them together.

Moreover, the results suggest the superior SIS accuracy of the BDS-3 satellites to the BDS-2 satellites. For most of the BDS-3 satellites, the  $\sigma_{\text{URA}}$  is about 1 meter when Definition a is considered. This mainly benefits from new spaceborne clocks and the equipped ISL payloads. The former helps improve the precision of short-term clock prediction, and the latter mitigates the challenges caused by the limited ground stations by enabling satellite-to-satellite communication and ranging.

Although Figures 16 and 18 also show the estimated fault probabilities of the BDS-3 satellites, we are not confident in these numbers because the fault probabilities of some satellites (e.g., C20, C29, and 30) are significantly influenced by some prolonged (e.g., over 10 hours) faults. And the long fault duration may be attributed to the maturation phase that BDS-3 has been undergoing. It is reasonable to expect that the fault duration will not be such long after this phase. Please also note that the current results may not provide a fully reliable picture of the future BDS-3 SIS performance. This is because, first, there might be some satellite faults during the data outages. Second, the



**FIGURE 14** The estimated values of URA and fault probability ( $P$ ) for BDS-2 IGSO satellites, where the black dashed lines indicate Definition a and the red solid lines denote Definition b [Color figure can be viewed in the online issue, which is available at [wileyonlinelibrary.com](http://wileyonlinelibrary.com) and [www.ion.org](http://www.ion.org)]

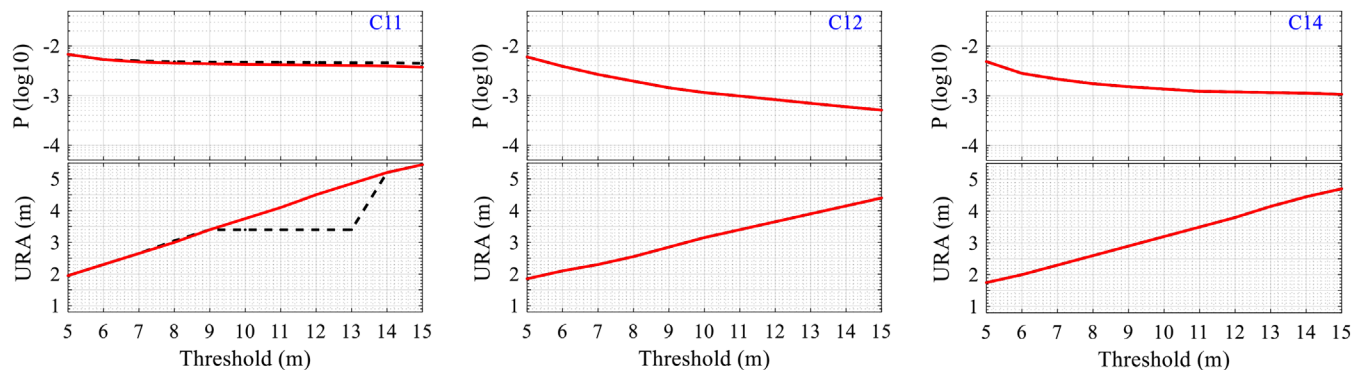
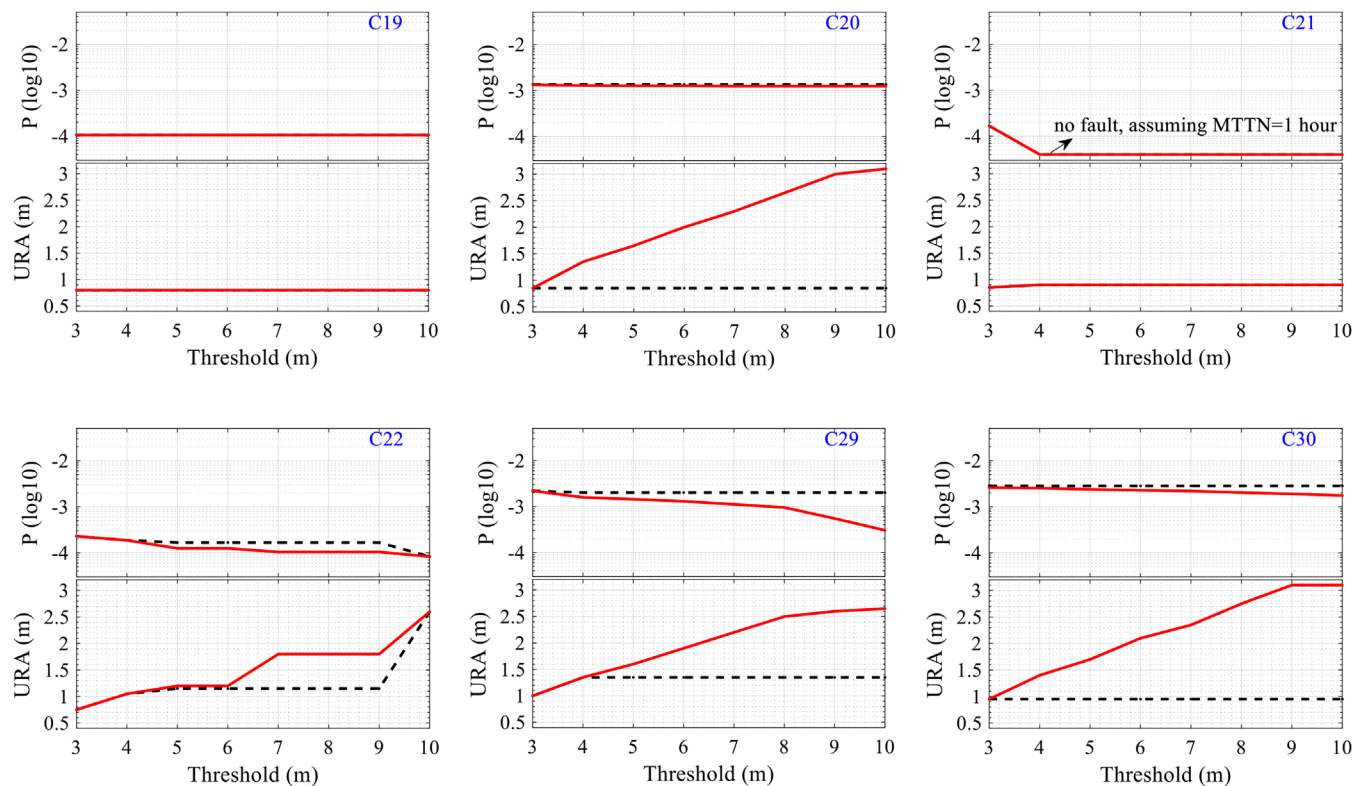


**FIGURE 15** The estimated values of URA and fault probability ( $P$ ) for BDS-2 MEO satellites, where the black dashed lines indicate Definition a and the red solid lines denote Definition b [Color figure can be viewed in the online issue, which is available at [wileyonlinelibrary.com](http://wileyonlinelibrary.com) and [www.ion.org](http://www.ion.org)]

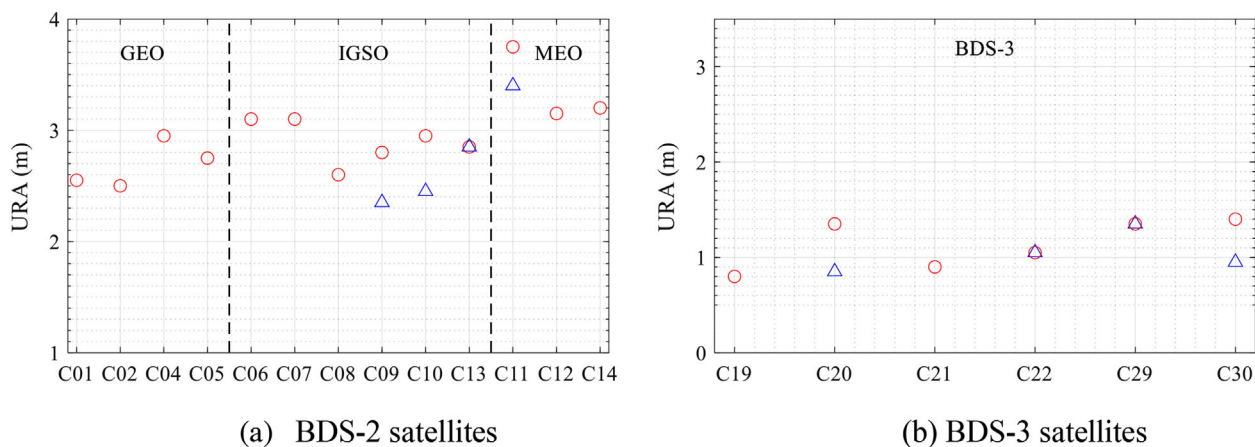
data volume is not sufficiently large for a robust evaluation. Moreover, the integrity performance may be significantly improved after the constellation becomes mature. Therefore, it is reasonable that BDS-3 can make commitments into the SARPs with better performance than the results obtained in this work. Toward making BDS-3 available to ARAIM users, we will continuously conduct performance monitoring for BDS-3 in future work.

Figure 19 shows the observed fault rates of each monitored satellite. Note that, the fault rate is exactly the same under the two fault definitions because they only impact the fault duration. The preliminary results suggest that the fault rate varies from  $1.3 \times 10^{-4}$  to  $10^{-3}$  per hour among different BDS-2 satellites and ranges from  $4 \times 10^{-5}$  (0 fault in 1.5 years) to  $3.5 \times 10^{-4}$  (4 faults in 1.5 years) per hour for BDS-3 satellites. Besides, there are no concurrent faults





**FIGURE 16** The estimated values of URA and fault probability ( $P$ ) for BDS-3 satellites, where the black dashed lines indicate Definition a and the red solid lines denote Definition b [Color figure can be viewed in the online issue, which is available at [wileyonlinelibrary.com](http://wileyonlinelibrary.com) and [www.ion.org](http://www.ion.org)]

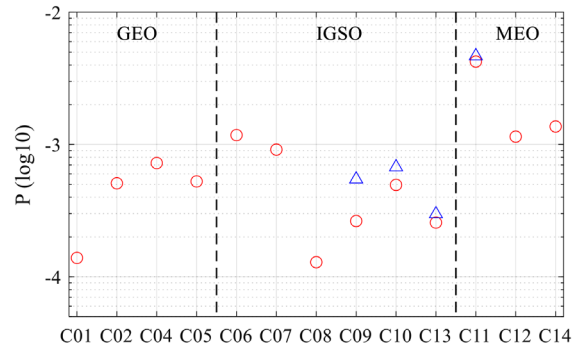


**FIGURE 17** URA values of various satellites, where triangles indicate Definition a and circles denote Definition b [Color figure can be viewed in the online issue, which is available at [wileyonlinelibrary.com](http://wileyonlinelibrary.com) and [www.ion.org](http://www.ion.org)]

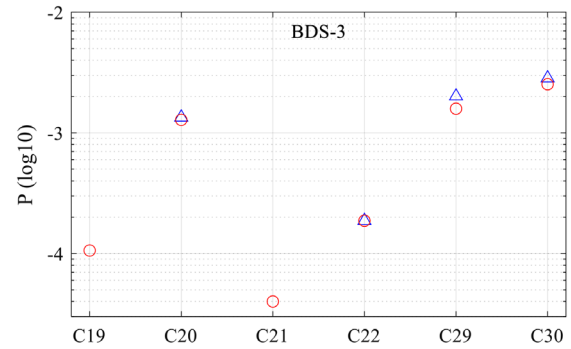
and thereby no constellation fault observed in the dataset of BDS-2 and BDS-3. Based on Equation (7) (Walter et al., 2019), the constellation fault rate can therefore be preliminarily set to  $1.3 \times 10^{-5}$  per hour for BDS-2 and  $4 \times 10^{-5}$  per hour for BDS-3. We cannot provide the estimate of constellation fault probability because the MTTN of constellation faults is unknown. This result is obtained by assuming that

there is no constellation fault hidden in the missing data. We will examine this assumption and update the result (if necessary) in future work.

Due to the limited data volume of BDS-3, we will only focus on BDS-2 in the following analyses. MTTN is an important performance indicator of a navigation system, which shows how quickly it can respond to an SIS fault.

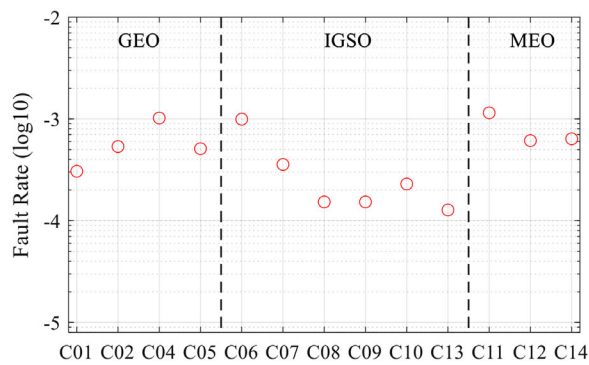


(a) BDS-2 satellites

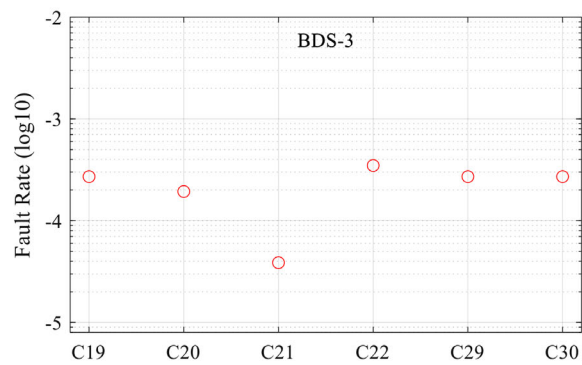


(b) BDS-3 satellites

**FIGURE 18** Fault probabilities for various satellites, where triangles indicate Definition a and circles denote Definition b [Color figure can be viewed in the online issue, which is available at [wileyonlinelibrary.com](http://wileyonlinelibrary.com) and [www.ion.org](http://www.ion.org)]



(a) BDS-2 satellites

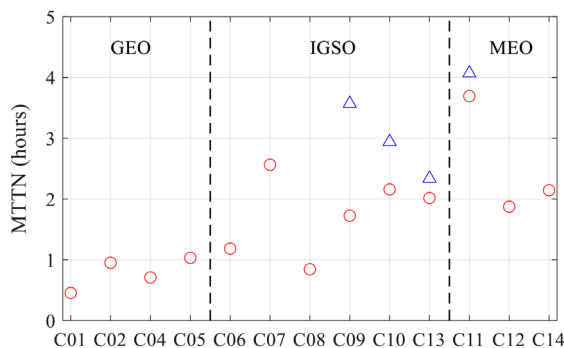


(b) BDS-3 satellites

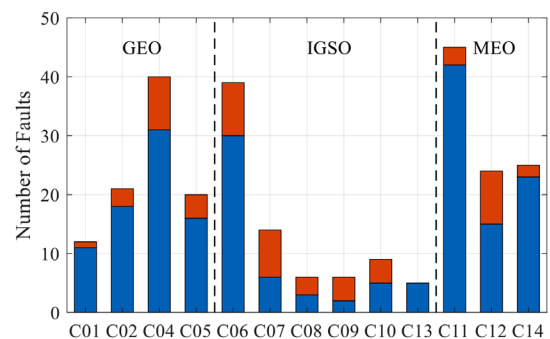
**FIGURE 19** Estimated fault rates for BDS-2 and BDS-3 satellites [Color figure can be viewed in the online issue, which is available at [wileyonlinelibrary.com](http://wileyonlinelibrary.com) and [www.ion.org](http://www.ion.org)]

Figure 21 presents the preliminary estimates of MTTN for each BDS-2 satellite. The MTTN values here are simply estimated by calculating the average fault duration. As can be seen, for most of the satellites, the MTTN appears to

be below 2.5 hours under Definition b and below 3 hours under Definition a. However, there is also an obvious variation in this number among different satellites: the MTTN varies from 30 minutes (C01) to about 4 hours (C11).



**FIGURE 20** Estimated MTTN for BDS-2 satellites, where triangles indicate Definition a and circles denote Definition b [Color figure can be viewed in the online issue, which is available at [wileyonlinelibrary.com](http://wileyonlinelibrary.com) and [www.ion.org](http://www.ion.org)]



**FIGURE 21** The fault sources of BDS-2 satellites, where the bottom indicates clock and the top denotes orbit [Color figure can be viewed in the online issue, which is available at [wileyonlinelibrary.com](http://wileyonlinelibrary.com) and [www.ion.org](http://www.ion.org)]

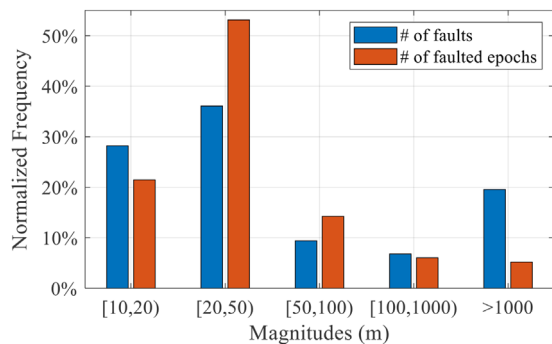


**FIGURE 22** The relative frequency histogram of the maximum magnitudes of BDS-2 SIS faults [Color figure can be viewed in the online issue, which is available at [wileyonlinelibrary.com](http://wileyonlinelibrary.com) and [www.ion.org](http://www.ion.org)]

On the whole, the GEOs have the lowest MTTN while the MEOs have the longest one. This figure also suggests that the MTTN is impacted by the fault definition, and this is because the fault duration is extended under Definition a.

However, the above MTTN estimation method may not provide a reliable estimate with sufficient accuracy for the following reasons. First, the number of observed faults is not large enough to accurately capture the SIS fault characteristics. Second, the calculation relies on the assumptions that (a) the duration of a fault is at least 15 minutes and (b) a fault occurring in one time interval does not affect the faults occurring in any other intervals, but both of them may not be true. Besides, the individual fault durations for the MEOs would be significantly affected by when the fault initiates compared to the visibility of the ground monitoring stations. Therefore, the results in Figure 20 are preliminary and should be further examined in the future. Integrity Failure Modes and Effects Analysis (IFMEA) is an effective approach to help assess the MTTN, which intends to identify satellite failure modes, determine their probability of occurrence, and analyze their effects on the users (Ober & Harriman, 2006). Therefore, we provide some initial assessments on the fault characteristics of BDS-2 as follows. In future work, more efforts will be taken to complete the IFMEA for BDS and to further assess the MTTN with the analysis results.

Figure 21 summarizes the sources of the observed BDS-2 SIS faults, and Figure 22 presents the relative frequency histogram of their maximum magnitudes. The results indicate that over 70% of the SIS faults are attributed to the clock component. Clock anomalies even occupy more than 88% for MEOs, while this proportion is only about 50% for GEOs and IGSOs on the whole. As for the fault magnitude, Figure 22 suggests that the magnitude of most faults is below 100 meters, although large (over 1 kilometer) faults also account for a significant proportion.

## 6 | CONCLUSIONS

This work characterizes the BDS-2 and BDS-3 SIS performance from the integrity perspective. Using our newly proposed SISRE evaluation scheme, we analyze the 4.5-year (from the year 2016 to mid-2020) data for BDS-2 and the recent 1.5-year data from 2019 for BDS-3. The main contribution is producing the preliminary estimates on URA ( $\sigma_{\text{URA}}$ ) and fault probability for individual satellites. The following conclusions are drawn in this study.

The definition of SIS faults can impact the evaluation on integrity performance. Under a new definition where the below-threshold segment of a ramp fault is considered faulted,  $\sigma_{\text{URA}}$  tends to decrease at the cost of increased fault probability. For some satellites, this new definition and the traditional deterministic one can yield significantly different results, although this strong difference may be due to the limited data volume. Besides, the detection threshold is another factor that affects the estimates of ISM parameters. The increased threshold potentially results in an increase in URA and a decrease in fault probability, but this trend will disappear once the threshold is large enough.

This work preliminarily evaluates the SIS performance of individual BDS-2 satellites. Under a 10-meter threshold, most of the BDS-2 satellites hold the  $\sigma_{\text{URA}}$  of 2.4~3.2 meters, except C11 whose  $\sigma_{\text{URA}}$  is greater than 3.4 meters. Their fault probabilities also vary noticeably with a range from  $1.5 \times 10^{-4}$  (C01 and C08) to  $4.5 \times 10^{-3}$  (C11). And the associated fault rates generally range from  $10^{-4}$  to  $10^{-3}$  per hour. Besides, initial results indicate that the MTTN of most satellites is below 2.5 hours under Definition a and below 3 hours under Definition b. However, individual fault duration could range from below 15 minutes to 18 hours.

The integrity performance of BDS-3 is also initially evaluated by involving the recent 1.5-year data for 6 satellites. The results suggest the superior SIS accuracy of the BDS-3 satellites to the BDS-2 satellites. Under a 4-meter threshold, most of the analyzed satellites hold the  $\sigma_{\text{URA}}$  of about 1 meter when Definition a is considered. And their fault rates range from  $4 \times 10^{-5}$  to  $3.5 \times 10^{-4}$  per hour. The estimated fault probability and MTTN are not provided here because they may be significantly influenced by some prolonged faults. This might result from the maturation phase that BDS-3 has been undergoing, and it is expected that the fault duration will not be such long after this phase. And because of this phase, the current results may not well represent future BDS-3 performance. Therefore, it is reasonable that BDS-3 can make commitments into the SARPs with better performance than the results here.

These results demonstrate the considerable variability in performance over satellites, even for those belonging to the




same type. Therefore, it is strongly suggested to set different values for each satellite in the ISM. It is also worth mentioning that there are no concurrent faults (i.e., no constellation fault) observed in the datasets of BDS-2 and BDS-3. Based on Equation (7), the constellation fault rate can therefore be preliminarily set to  $1.3 \times 10^{-5}$  per hour for BDS-2 and  $4 \times 10^{-5}$  per hour for BDS-3. We cannot provide the estimate of constellation fault probability because the MTTN of constellation faults is unknown.

Finally, it is important to remember that all the results above can only be viewed as preliminary. They are obtained under the assumption that there is no satellite/constellation fault in the absence of broadcast and precise ephemerides. Given the relatively frequent data outages, i.e., over 1% for each BDS-2 satellite and over 6% for each BDS-3 satellite, this assumption must be examined in future work, and the results should be updated if necessary. Besides, we are not confident that the past data can necessarily represent future performance, especially given the limited data volume and the possibly nonstationary performance. Moreover, it is observed that different fault definitions and thresholds could lead to a considerable difference in the results, and we do not know which set of estimates can best predict future performance. In this regard, it would be better to confirm the official commitments rather than to set values based on the historical data. It is expected that the commitments of BDS will be available soon, and thus, continuous efforts should be devoted to confirming them in the future.

## ACKNOWLEDGEMENT

We express our gratitude to the anonymous reviewers and editors for their insightful and critical comments. This work is supported by China Postdoctoral Science Foundation (Grant No. 2019M661511). Thanks are due to IGS MGEX, WHU, GFZ, TARC, and APM of CAS for providing the broadcast and precise ephemerides. We are, furthermore, grateful to Dr. Oliver Montenbruck (DLR), Dr. Jing Guo (WHU), Dr. Kaifa Kuang (WHU), Dr. Zhiguo Deng (GFZ), Dr. Changjiang Geng (TARC), and Dr. Haitao Wang (APM of CAS) for providing some necessary knowledge on the broadcast and precise products. The authors would also like to thank Dr. Todd Walter (Stanford University) for our discussions on overbounding techniques.

## ORCID

Shizhuang Wang  <https://orcid.org/0000-0003-3518-2281>  
Yawei Zhai  <https://orcid.org/0000-0002-6552-5903>  
Xingqun Zhan  <https://orcid.org/0000-0002-7655-067X>

## REFERENCES

- Blanch, J., Walter, T., Enge, P., Lee, Y., Pervan, B., Rippl, M., ... Kropp, V. (2015). Baseline advanced RAIM user algorithm and possible improvements. *IEEE Transactions on Aerospace and Electronic Systems*, 51(1), 713–732. <https://doi.org/10.1109/TAES.2014.130739>
- Blanch, J., Walter, T., & Enge, P. (2018). Gaussian bounds of sample distributions for integrity analysis. *IEEE Transactions on Aerospace and Electronic Systems*, 55(4), 1806–1815. <https://doi.org/10.1109/TAES.2018.2876583>
- China Satellite Navigation Office. (2019a). *BeiDou navigation satellite system signal in space interface control document open service signal B1I (Version 3.0)*. <http://en.beidou.gov.cn/SYSTEMS/Officialdocument/>
- China Satellite Navigation Office. (2019b). *Development of the BeiDou navigation satellite system (Version 4.0)*. <http://en.beidou.gov.cn/SYSTEMS/Officialdocument/>
- China Satellite Navigation Office. (2019c). *Satellite antenna phase center of BDS*. <http://en.beidou.gov.cn/SYSTEMS/Officialdocument/>
- DeCleene, B. (2000, September). Defining pseudorange integrity - Overbounding. *Proceedings of the 13th International Technical Meeting of the Satellite Division of The Institute of Navigation (ION GPS 2000)*, Salt Lake City, UT, 1916–1924.
- Dilssner, F., Springer, T., Schönmann, E., & Enderle, W. (2014, June). Estimation of satellite antenna phase center corrections for BeiDou. *Proceedings of IGS Workshop*, Pasadena, CA, 23–27.
- DoD. (2008). *Global positioning system standard positioning service performance standard* (4th edition). <https://www.gps.gov/technical/ps/2008-SPS-performance-standard.pdf>
- Gunning, K., Walter, T., & Enge, P. (2018, September). Multi-GNSS constellation anomaly detection and performance monitoring. *Proceedings of the 30th International Technical Meeting of the Satellite Division of The Institute of Navigation (ION GNSS+ 2017)*, Portland, OR, 1051–1062. <https://doi.org/10.33012/2017.15174>
- Heng, L., Gao, G. X., Walter, T., & Enge, P. (2011, January). Statistical characterization of GPS signal-in-space errors. *Proceedings of the 2011 International Technical Meeting of The Institute of Navigation*, San Diego, CA, 312–319.
- Heng, L., Gao, G. X., Walter, T., & Enge, P. (2012). GPS signal-in-space integrity performance evolution in the last decade. *IEEE Transactions on Aerospace and Electronic Systems*, 48(4), 2932–2946. <https://doi.org/10.1109/TAES.2012.6324670>
- IGS MGEX. (2020a). *IGS MGEX products*. [http://mgex.igs.org/IGS\\_MGEX\\_Products.php](http://mgex.igs.org/IGS_MGEX_Products.php)
- IGS MGEX. (2020b). *IGS official antenna correction file (igs14.atx)*. <ftp://igs.org/pub/station/general/>
- Larson, J. D. (2018). *Gaussian-Pareto overbounding: A method for managing risk in safety-critical navigation systems* (Doctoral dissertation). [https://conservancy.umn.edu/bitstream/handle/11299/200312/Larson\\_umn\\_0130E\\_19437.pdf?isAllowed=y&sequence=1](https://conservancy.umn.edu/bitstream/handle/11299/200312/Larson_umn_0130E_19437.pdf?isAllowed=y&sequence=1)
- Lv, Y., Geng, T., Zhao, Q., & Liu, J. (2018). Characteristics of BeiDou-3 experimental satellite clocks. *Remote Sensing*, 10(11), 1847. <https://doi.org/10.3390/rs10111847>
- Lv, Y., Geng, T., Zhao, Q., Xie, X., & Zhou, R. (2020). Initial assessment of BDS-3 preliminary system signal-in-space range error. *GPS Solutions*, 24(1), 1–13. <https://doi.org/10.1007/s10291-019-0928-x>
- Martini, I., & Sgammini, M. (2019, September). Integrity support message generation algorithms prototype. *Proceedings of the 32nd International Technical Meeting of the Satellite Division of The*



- Institute of Navigation (ION GNSS+ 2019), Miami, FL, 552–572. <https://doi.org/10.33012/2019.16866>
- Martini, I., Sgammini, M., & Boyero, J. P. (2020a, September). Error bounding for ARAIM integrity support message generation. *Proceedings of the 33rd International Technical Meeting of the Satellite Division of The Institute of Navigation (ION GNSS+ 2020)*, 1068–1088. <https://doi.org/10.33012/2020.17577>
- Martini, I., Sgammini, M., & Boyero, J. P. (2020b). Galileo model of group delay accuracy for advanced RAIM users. *NAVIGATION*, 67(1), 129–141. <https://doi.org/10.1002/navi.356>
- Montenbruck, O., Schmid, R., Mercier, F., Steigenberger, P., Noll, C., Fatkulov, R., ... Ganeshan, A. S. (2015). GNSS satellite geometry and attitude models. *Advances in Space Research*, 56(6), 1015–1029. <https://doi.org/10.1016/j.asr.2015.06.019>
- Montenbruck, O., Steigenberger, P., & Hauschild, A. (2015). Broadcast versus precise ephemerides: A multi-GNSS perspective. *GPS Solutions*, 19(2), 321–333. <https://doi.org/10.1007/s10291-014-0390-8>
- Montenbruck, O., Steigenberger, P., & Hauschild, A. (2018). Multi-GNSS signal-in-space range error assessment – Methodology and results. *Advances in Space Research*, 61(12), 3020–3038. <https://doi.org/10.1016/j.asr.2018.03.041>
- Montenbruck, O., Steigenberger, P., Prange, L., Deng, Z., Zhao, Q., Perosanz, F., ... Schaer, S. (2017). The multi-GNSS experiment (MGEX) of the international GNSS service (IGS) – Achievements, prospects and challenges. *Advances in Space Research*, 59(7), 1671–1697. <https://doi.org/10.1016/j.asr.2017.01.011>
- Ober, P. B., & Harriman, D. (2006, September). On the use of multiconstellation-RAIM for aircraft approaches. *Proceedings of the 19th International Technical Meeting of the Satellite Division of The Institute of Navigation (ION GNSS 2006)*, Fort Worth, TX, 2587–2596.
- Ouyang, C., Shi, J., Shen, Y., & Li, L. (2019). Six-year BDS-2 broadcast navigation message analysis from 2013 to 2018: Availability, anomaly, and SIS UREs assessment. *Sensors (Switzerland)*, 19(12). <https://doi.org/10.3390/s19122767>
- Perea, S., Meurer, M., Martini, I., Rippl, M., & Pervan, B. (2018, September). ARAIM ground architecture based on GNSS monitoring infrastructures. *Proceedings of the 30th International Technical Meeting of the Satellite Division of The Institute of Navigation (ION GNSS+ 2017)*, Portland, OR, 1008–1018. <https://doi.org/10.33012/2017.15281>
- Perea, S., Meurer, M., Rippl, M., Belabbas, B., & Joerger, M. (2017). URA/SISA analysis for GPS and galileo to support ARAIM. *NAVIGATION*, 64(2), 237–254. <https://doi.org/10.1002/navi.199>
- Rife, J., Pullen, S., Enge, P., & Pervan, B. (2006). Paired overbounding for nonideal LAAS and WAAS. *IEEE Transactions on Aerospace and Electronic Systems*, 42(4), 1386–1395. <https://doi.org/10.1109/TAES.2006.314579>
- Rife, J., Walter, T., & Blanch, J. (2004, December). Overbounding SBAS and GBAS error distributions with excess-mass functions. *Proceedings of the 2004 International Symposium on GNSS/GPS*, Sydney, Australia.
- Walter, T., & Blanch, J. (2015, April). KEYNOTE - Characterization of GPS clock and ephemeris errors to support ARAIM. *Proceedings of the ION 2015 Pacific PNT Meeting*, Honolulu, HI, 920–931.
- Walter, T., Blanch, J., & Gunning, K. (2019, April). Standards for ARAIM ISM data analysis. *Proceedings of the ION 2019 Pacific PNT Meeting*, Honolulu, HI, 777–784. <https://doi.org/10.33012/2019.16837>
- Walter, T., Blanch, J., Joerger, M., & Pervan, B. (2019). Determination of fault probabilities for ARAIM. *IEEE Transactions on Aerospace and Electronic Systems*, 55(6), 3505–3516. <https://doi.org/10.1109/TAES.2019.2909727>
- Walter, T., Gunning, K., Eric Phelts, R., & Blanch, J. (2018). Validation of the unfaulted error bounds for ARAIM. *NAVIGATION*, 65(1), 117–133. <https://doi.org/10.1002/navi.214>
- Wang, B., Chen, J., Wang, B., & Zhou, J. (2018, October). Signal-in-space accuracy analysis for BDS in 2016–2017. *Proceedings of IGS Workgroup 2018*, Wuhan, China, 1–15.
- Wang, X., & Du, Y. (2018). BDT performance and time offset analysis. *Journal of Physics: Conference Series*, 1060(1). <https://doi.org/10.1088/1742-6596/1060/1/012003>
- Wang, Z., Shao, W., Li, R., Song, D., & Li, T. (2018). Characteristics of BDS signal-in-space user ranging errors and their effect on advanced receiver autonomous integrity monitoring performance. *Sensors (Switzerland)*, 18(12). <https://doi.org/10.3390/s18124475>
- Wu, Y., Liu, X., Liu, W., Ren, J., Lou, Y., Dai, X., & Fang, X. (2017). Long-term behavior and statistical characterization of BeiDou signal-in-space errors. *GPS Solutions*, 21(4), 1907–1922. <https://doi.org/10.1007/s10291-017-0663-0>
- Yang, H., Xu, T., Nie, W., Gao, F., & Guan, M. (2019). SLR validation and evaluation on BDS precise orbits from 2013 to 2018. *Advances in Space Research*, 64(2), 475–490. <https://doi.org/10.1016/j.asr.2019.04.030>
- Yang, Y., Gao, W., Guo, S., Mao, Y., & Yang, Y. (2019). Introduction to BeiDou-3 navigation satellite system. *NAVIGATION*, 66(1), 7–18. <https://doi.org/10.1002/navi.291>
- Zhu, N., Marais, J., Betaille, D., & Berbineau, M. (2018). GNSS position integrity in urban environments: A review of literature. *IEEE Transactions on Intelligent Transportation Systems*, 19(9), 2762–2778. <https://doi.org/10.1109/TITS.2017.2766768>

**How to cite this article:** Wang S, Zhai Y, Zhan X. Characterizing BDS Signal-in-Space Performance from Integrity Perspective. *NAVIGATION*. 2021;68:157–183. <https://doi.org/10.1002/navi.409>

## APPENDIX A

This appendix offers some further analyses on the absence of precise products, including their effects and underlying causes. It also gives some preliminary results based on a PCE-free anomaly detection method.

As shown in Figures 1–4, a substantial number (over 1%) of precise ephemerides are missing, although two independent products are employed to supplement each other. This is extremely harmful for the assessment on fault probability because the anomalies may be hidden over these periods. According to J. Guo (Private communication, August 1, 2020), the MGEX ACs tend to simply not output the precise ephemeris of a satellite for one day if the satellite encounters orbital maneuvers or other issues that cause discontinuity. But this does not mean that there is likely to be a fault on that day, because the maneuvers are often

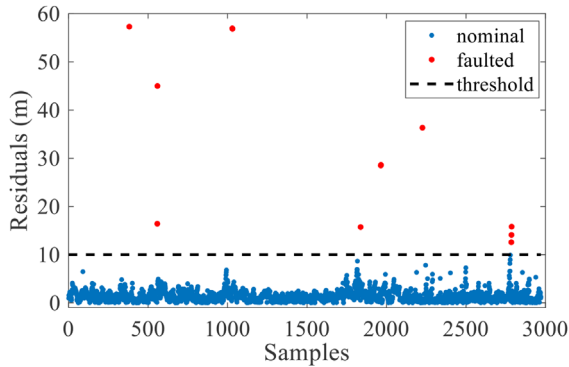


**FIGURE A1** Anomaly detection for C01 in the absence of PCEs (threshold: 10 meters) [Color figure can be viewed in the online issue, which is available at [wileyonlinelibrary.com](http://wileyonlinelibrary.com) and [www.ion.org](http://www.ion.org)]

scheduled and the satellite will be set to “unhealth” over the operational period.

To produce more reliable estimates on fault probability, it is important to perform anomaly detection in the absence of PCEs. For this purpose, Gunning et al. (2018) presented an anomaly detection scheme based on raw observations. In this scheme, the pseudorange residuals are selected as the test statistics, which are calculated by differencing the observed pseudoranges with the predicted ones (based on the ephemeris and the station location). Taking C01 as an example, Figure A1 provides the anomaly detection result involving all the epochs when the PCE is absent. The observations recorded in the HKWS station are employed for this analysis. The result suggests that ten faulted samples (seven faults) are observed over these periods. Please note, these samples are not considered in the results shown in Section 5. In future work, we will apply this method to all the monitored satellites and update the estimates of fault probability and fault rate accordingly.

## APPENDIX B

This appendix shows the relationship between SIS accuracy and AODs. As we know, the SIS accuracy may vary as a function of AODC and AODE. To examine this, this section provides a quantitative analysis on this relationship. First, Figures A2 and A3 show the number of samples as a function of AODC and AODE, respectively. The results suggest that for each of the GEO, IGSO, and BDS-3 satellites, the majority of the samples hold the same AODC and the same AODE. In contrast, the samples at some other AODs are not sufficient to be statistically meaningful.

Then, Figure A4 demonstrates the standard deviations (sigmas) of clock errors as a function of AODC, and Figures A5~A7 give the sigmas of orbital errors as a function of AODE. The results indicate that the variation in satellite clock accuracy with AODC is considerable for some satellites (mainly the BDS-2 MEOs) while not obvious for the

others. And the results also suggest that the variation in orbital accuracy with AODE is not so obvious as that in the clock component. Please note, the sigmas for some AODs are not calculated because the associated number of samples is too small (less than 200) to derive a reliable estimate. Besides, we perform the anomaly detection under Definition b and remove the faulted samples from the calculation of sigmas. The detection threshold is set to 10 meters for BDS-2 and 4 meters for BDS-3.

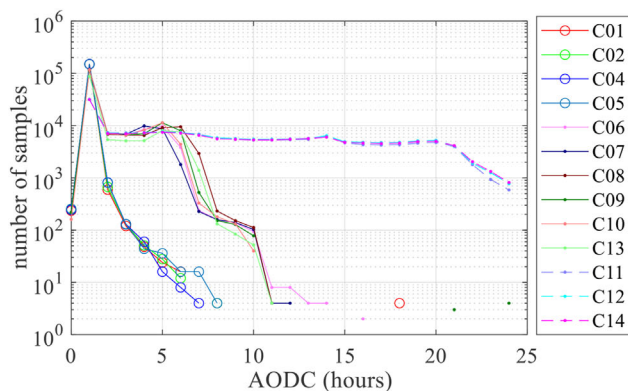
Finally, we provide some comments on BDS data partitioning by AODs. It is suggested to partition the data by AODs if the SIS accuracy is highly dependent on them. However, this partition may not be feasible in practice. As shown above, the samples at some AODs are too few to be statistically meaningful. Moreover, for most of the BDS satellites, it seems to be not strictly necessary to do the partition because the variation in SIS accuracy with AODs is not significantly considerable. In future work, more efforts will be devoted to addressing the data partition problem, especially to studying how to account for the variation shown above in the offline ISM generation process and in the online ARAIM operations.

## APPENDIX C

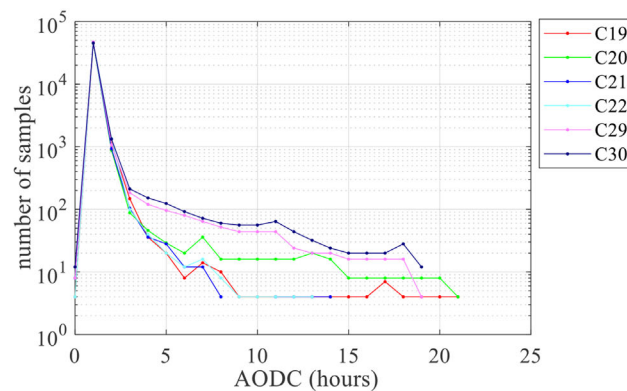
This section provides some additional BDS SISRE characteristics for each satellite and offers an accuracy comparison among them. First, Figure A8 gives the MPE time series for each monitored satellite. In the subfigures, the y-axis is limited to  $\pm 25$  meters for BDS-2 and  $\pm 15$  meters for BDS-3. This figure can not only demonstrate the nominal SISRE behaviors of each satellite but depict the occurrences of ramp faults. This figure also shows the standard deviation of MPE ( $\sigma_{\text{MPE}}$ ) for each satellite, which is calculated by using a 20-meters threshold to filter out large errors.

Then, Figure A9 shows the error distributions of each satellite in the form of relative frequency histogram (RFH). An RFH is a normalized frequency histogram by the number of total samples, and it acts as an estimation of the probability density function (PDF). For most satellites (except the GEOs), the core error distributions of each component appear to be nearly Gaussian. These error distributions are also approximately unimodal and symmetric. As stated in Section 2.4, the IURE distribution for every user will also have these good properties if the user-grid URE metric is adopted.

It is necessary to remember that the FCDF overbounding approach (or other single-CDF approaches) imposes some requirements on the distributions to be bounded, i.e., the distribution needs to be zero-mean, zero-median, symmetric, and unimodal. As shown above, the actual distributions of most BDS satellites roughly satisfy these requirements, and thus, it can be initially considered

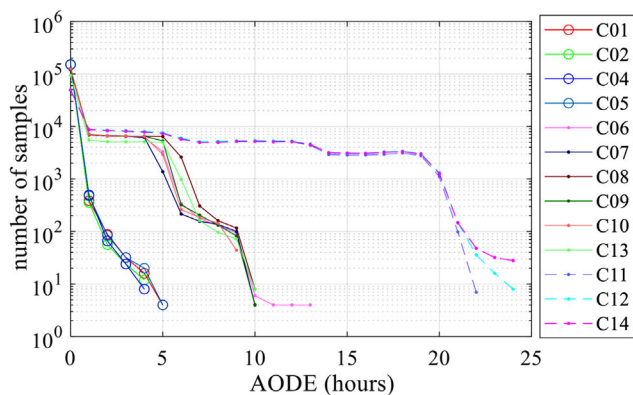


(a) BDS-2

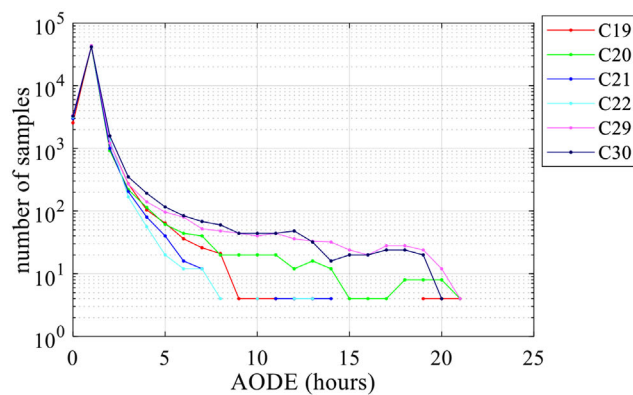


(b) BDS-3

**FIGURE A2** The number of samples as a function of AODC [Color figure can be viewed in the online issue, which is available at [wileyonlinelibrary.com](http://wileyonlinelibrary.com) and [www.ion.org](http://www.ion.org)]

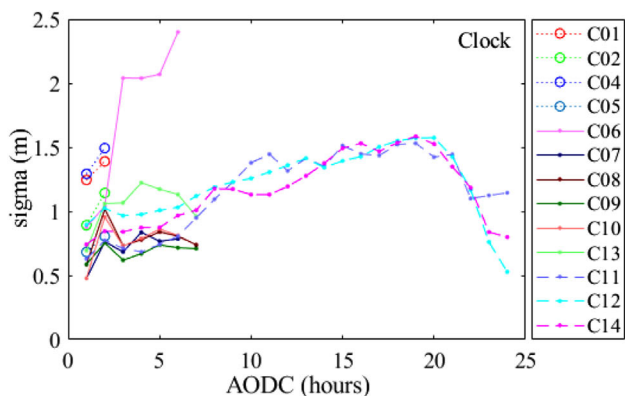


(a) BDS-2

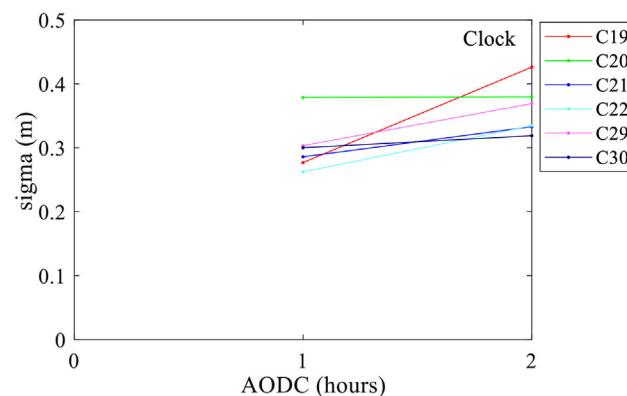


(b) BDS-3

**FIGURE A3** The number of samples as a function of AODE [Color figure can be viewed in the online issue, which is available at [wileyonlinelibrary.com](http://wileyonlinelibrary.com) and [www.ion.org](http://www.ion.org)]

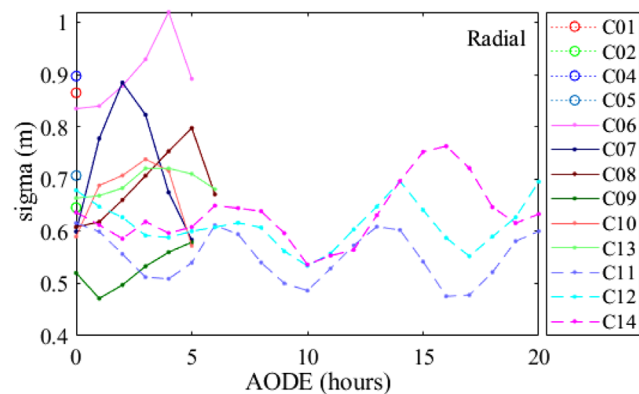


(a) BDS-2

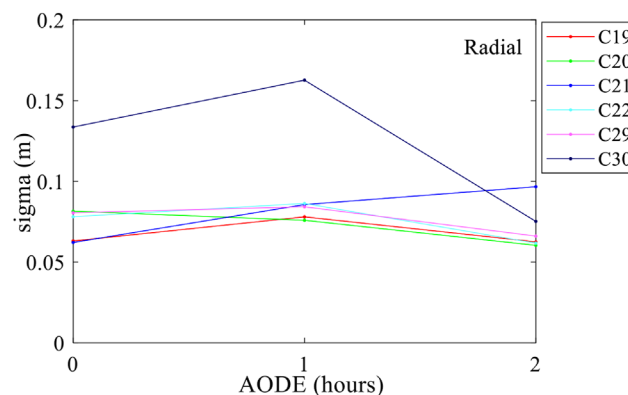


(b) BDS-3

**FIGURE A4** The standard deviation of clock errors as a function of AODC [Color figure can be viewed in the online issue, which is available at [wileyonlinelibrary.com](http://wileyonlinelibrary.com) and [www.ion.org](http://www.ion.org)]

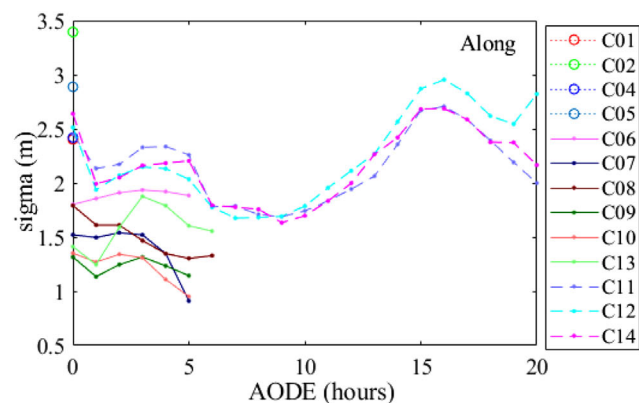


(a) BDS-2

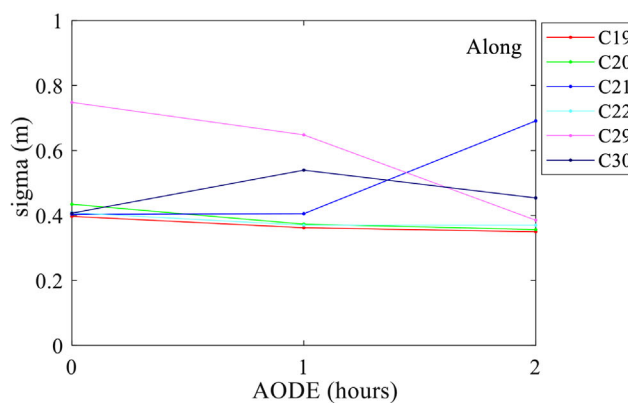


(b) BDS-3

**FIGURE A5** The standard deviation of radial errors as a function of AODE [Color figure can be viewed in the online issue, which is available at [wileyonlinelibrary.com](http://wileyonlinelibrary.com) and [www.ion.org](http://www.ion.org)]

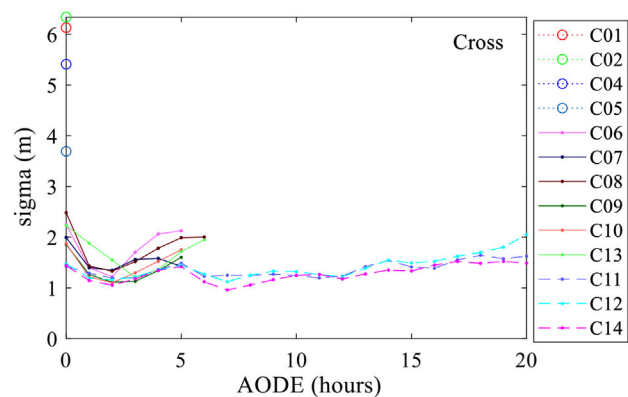


(a) BDS-2

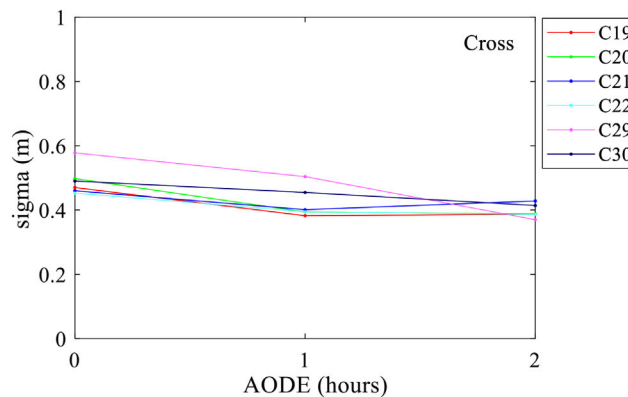


(b) BDS-3

**FIGURE A6** The standard deviation of along-track errors as a function of AODE [Color figure can be viewed in the online issue, which is available at [wileyonlinelibrary.com](http://wileyonlinelibrary.com) and [www.ion.org](http://www.ion.org)]



(a) BDS-2



(b) BDS-3

**FIGURE A7** The standard deviation of cross-track errors as a function of AODE [Color figure can be viewed in the online issue, which is available at [wileyonlinelibrary.com](http://wileyonlinelibrary.com) and [www.ion.org](http://www.ion.org)]



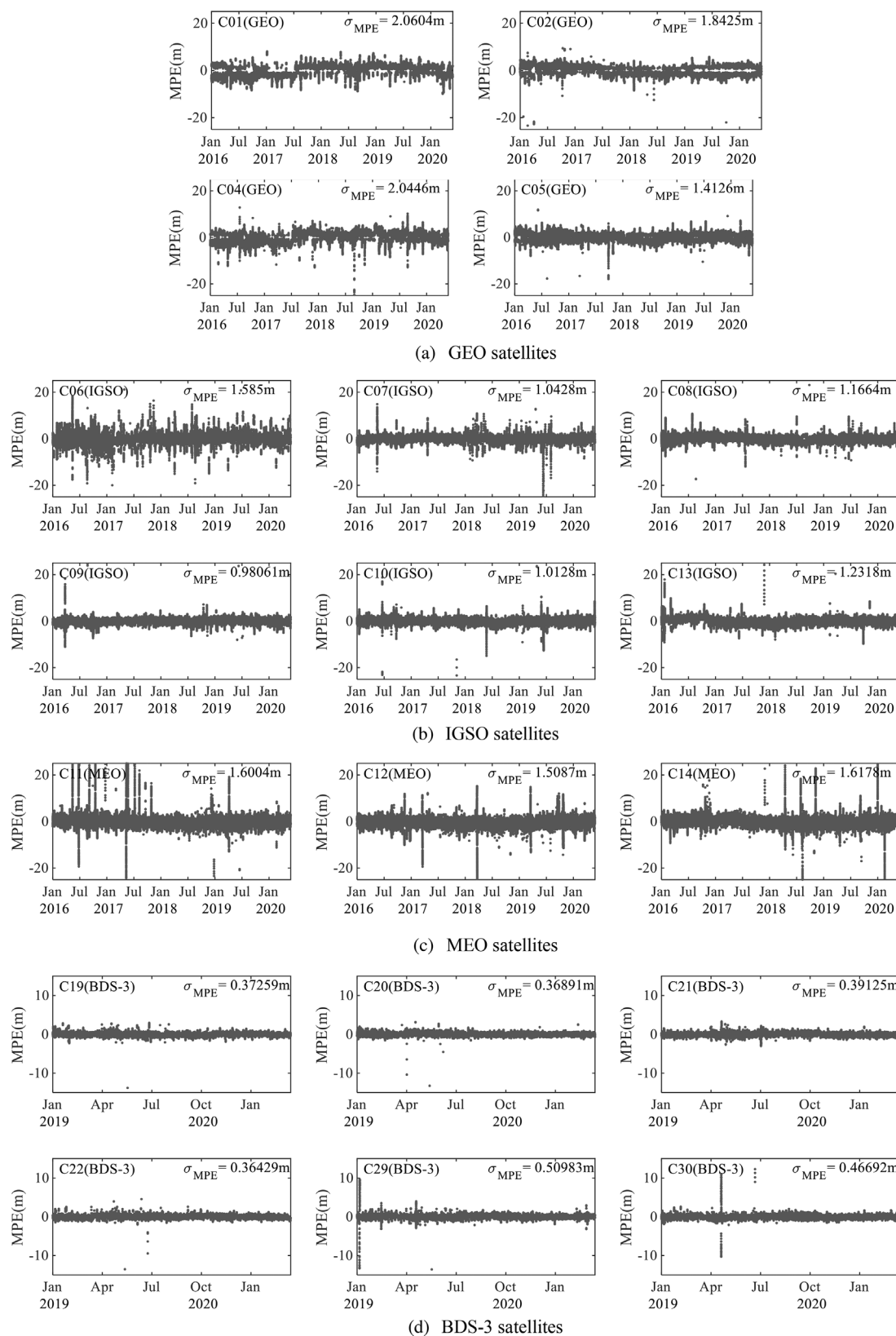
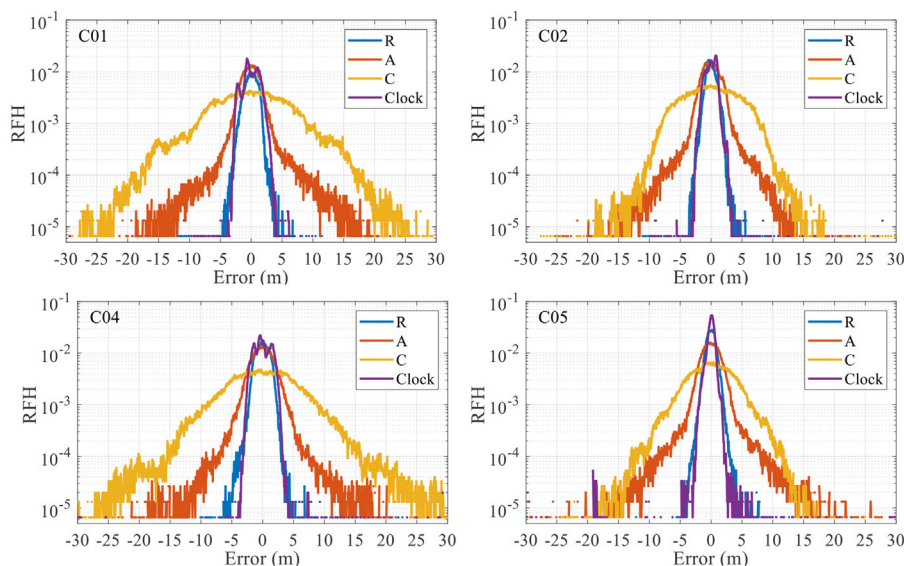
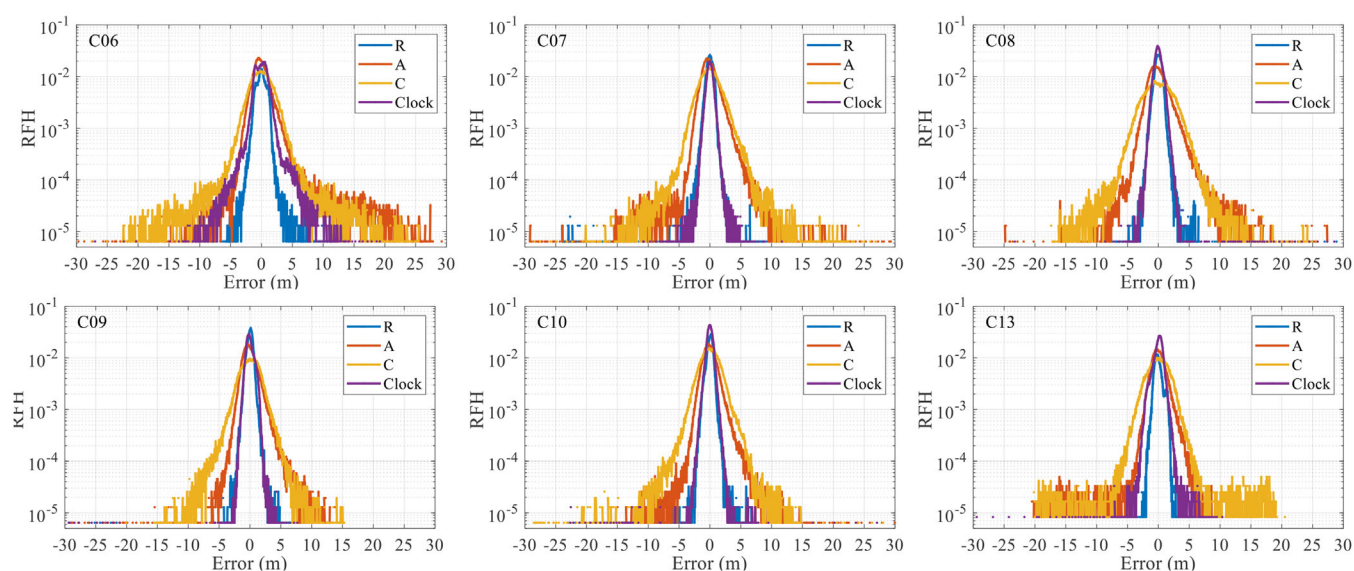


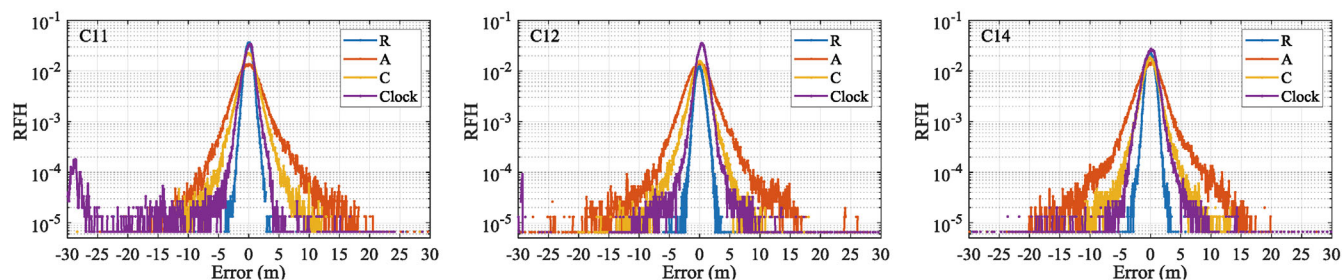
**FIGURE A8** The maximum projected error (MPE) time series for each satellite [Color figure can be viewed in the online issue, which is available at [wileyonlinelibrary.com](http://wileyonlinelibrary.com) and [www.ion.org](http://www.ion.org)]



(a) GEO satellites

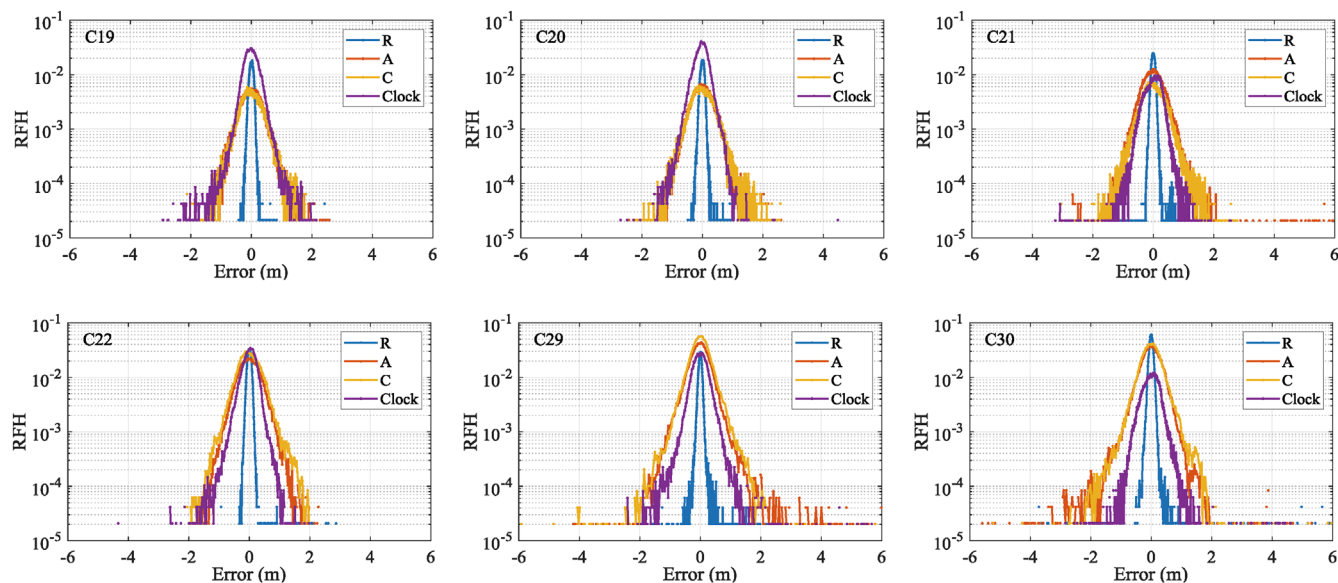


(b) IGSO satellites



(c) MEO satellites

**FIGURE A9** Radial (R), along-track (A), cross-track (C), and clock error distributions of BDS satellites. Please note, the x-axis is limited to  $\pm 30$  meters for BDS-2 and  $\pm 6$  meters for BDS-3 [Color figure can be viewed in the online issue, which is available at [wileyonlinelibrary.com](http://wileyonlinelibrary.com) and [www.ion.org](http://www.ion.org)]



(d) BDS-3 satellites

FIGURE A9 Continued

that the FCDF approach can be used for BDS data overbounding.

This figure also reveals that the clock error distributions of the GEOs and C06 appear to be multimodal. The cross-track error distributions of them are also obviously non-Gaussian, but this component only exerts a little effect on the SIS URE. In future work, we will investigate

the underlying causes of the abnormal phenomenon above. More importantly, we will examine whether the overbounding is still conservative after convolving the range-domain bounds into the position-domain bounds. More robust overbounding methods (e.g., paired overbounding and two-step overbounding) will also be employed to derive more reliable results.